

Goupil: A Monte Carlo engine for the backward transport of low-energy gamma-rays

Valentin Niess^{a,*}, Kinson Vernet^a, Luca Terray^{a,b}

^a *Université Clermont Auvergne, CNRS, LPCA, F-63000 Clermont-Ferrand, France.*

^b *Université Clermont Auvergne, CNRS, IRD, OPGC, Laboratoire Magmas et Volcans, F-63000 Clermont-Ferrand, France.*

Abstract

GOUPIL is a software library designed for the Monte Carlo transport of low-energy gamma-rays, such as those emitted from radioactive isotopes. The library is distributed as a Python module. It implements a dedicated backward sampling algorithm that is highly effective for geometries where the source size largely exceeds the detector size. When used in conjunction with a conventional Monte Carlo engine (i.e., GEANT4), the response of a scintillation detector to gamma-active radio-isotopes scattered over the environment is accurately simulated (to the nearest percent) while achieving events rates of a few kHz (with a ~ 2.3 GHz CPU).

PROGRAM SUMMARY

Program Title: Goupil

CPC Library link to program files: (to be added by Technical Editor)

Developer's repository link: <https://github.com/niess/goupil>

Code Ocean capsule: (to be added by Technical Editor)

Licensing provisions: LGPL-3.0

Programming language: C, Python and Rust.

Nature of problem: Backward Monte Carlo transport of gamma-rays that are emitted by mono-energetic sources distributed in space.

Solution method: A simple modification to a previously presented backward Monte Carlo algorithm [1].

References

- [1] V. Niess, A. Barnoud, C. Cârloganu, E. Le Ménédeu, Comput. Phys. Commun. 229 (2018) 54–67. <https://doi.org/10.1016/j.cpc.2018.04.001>.

Keywords: gamma-rays, Monte Carlo, transport, backward.

*Corresponding author

Email address: niess@in2p3.fr (Valentin Niess)

1. Introduction

The emission of gamma photons during the decay of radioactive isotopes offers a direct method of detecting radioactivity in the environment. Gamma photons have a long range as compared to other particles emitted by radionuclides, such as alpha particles and electrons. The observation of gamma photons at a specific location can indicate the presence of radioactivity at distances ranging from a few tens of centimetres in aquatic environments and soils to several hundred metres in the air. This property has been extensively studied in recent decades, making in-situ gamma-ray spectrometry (as opposed to laboratory gamma-ray spectrometry) one of the most widely used and accepted methods for the rapid identification and quantification of radionuclides in the environment. Gamma-ray measurements have numerous applications in the geosciences, such as mapping U-Th-K levels on continental surfaces (Grasty [1]), detecting radioactive contamination on land (Sanada and Torii [2]), the air (Grasty et al. [3]) or at sea (Povinec et al. [4]), measuring radon in the soil (Zafrir et al. [5]), the atmosphere (Baldoncini et al. [6]) or the hydrosphere (Dulai et al. [7]), studying the removal of aerosols by rain (Takeuchi and Katase [8]), and monitoring soil moisture (Reinhardt and Herrmann [9]). Thus, depending on the objectives being pursued, gamma-ray measurements are performed at -or below- ground level, from the atmosphere using a variety of aircraft, or underwater.

In a recent study, it has been shown that radon emissions accompanying volcanic outgassing can be very high, which may indicate internal variations in the volcano's plumbing system (Terray et al. [10]). Thus, it is important to have appropriate tools to continuously monitor radon outgassing into the atmosphere through volcanic gas plumes. Traditional techniques for measuring radon in the air rely on the detection of alpha particles, requiring a direct contact between the gas and the detector. However, due to the aggressive nature of the environment (high acidity and humidity), traditional techniques are unsuitable in this context. Therefore, as part of an interdisciplinary project combining volcanology and nuclear physics, we recently developed a ground-based (in-situ) gamma-ray spectrometer with a field of view covering $\sim 2\pi$ solid angle. Its purpose is to record the flux of descending gamma photons in an attempt to continuously monitor the activity of radon in the air volume above the volcano. A detailed description of this spectrometer will be given in a later article.

During this exploratory work, we faced the problem of modelling the transport of gamma photons from their emission regions to the spectrometer, which motivated the present work. Properly modelling gamma-rays transport is crucial in order to relate photon counts recorded in the spectrometer to concentrations of radionuclides in the environment. But, before discussing the details of this transport problem, let us first point out that we are only concerned with low-energy gamma-rays emitted by radionuclides, i.e. with energies less than a few MeV, as opposed e.g. to astrophysical gamma-rays which can reach energies of the order of TeV (resulting in extensive air showers, which are not addressed herein). Secondly, let us recall that, for most of the transport problem, gamma photons can be considered as point-like particles originating from incoherent sources and traveling in a straight line between two collisions with an atom of the propagation medium, where its direction might change significantly (see e.g. figure 1). Thirdly, note that a photon emitted at 1 MeV undergoes $\mathcal{O}(10)$ collisions before being definitively absorbed (by photoelectric effect).

The conventional approach to the present transport problem is to consider only those photons that have not interacted between their points of emission and detection, and that have been fully captured by the detector. This results in selecting the peaks in the measured energy spectrum corresponding to the emission lines of radioactive isotopes of interest. In this case, the transport between the source and the detector can be considered as rectilinear. The photon survival probability is calculated from the cross-section of all interaction processes (absorption and scattering) that may occur along the way (Minty [11]). This method, known as the point-kernel method, offers simple calculations but at the price of sacrificing a large amount of data. However, events statistics is often a limiting factor that one cannot afford to sacrifice.

In order to interpret full-spectrum data, i.e. including photo peaks and background resulting from scattered photons, it is necessary to model in detail the various interaction processes involved in the transport. For this purpose, Monte Carlo methods are commonly used due to the stochastic nature of collisions between a gamma photon and an atom. Monte Carlo methods represent the transport problem as a discrete set of likely trajectories, known as Monte Carlo realisations. The classical approach is to generate Monte Carlo realisations at frequencies consistent with the physical reality. This approach is usually called *analogue* Monte Carlo. The Monte Carlo method also allows for an accurate modelling of the detector response, resulting in synthetic-like measurements. Various codes, including GEANT4 [12–14] and MCNP [15], have been employed for interpreting full-spectrum data (Bagatelas et al. [16], Androurakaki et al. [17]).

Analogous Monte Carlo methods are effective when the photon’s source size is not large as compared to the detector size (typically only ten centimetres). For instance, this is the case in dense environments like water or soil, where the range of gamma-rays is usually less than one metre. In contrast, the mean free path between two collisions in air is large, approximately 100 m for a 1 MeV photon. Therefore, a gamma-ray detector placed in the air is sensitive to a large number of distant photons, but having a small probability of actually reaching the spectrometer. Analogous Monte Carlo methods require simulating all these trajectories, which is particularly inefficient in the air, since most simulated photons do not reach the detector.

Several solutions have been proposed to overcome this obstacle. For a ground-atmosphere interface with an (xOy) symmetry plane, and a gamma-ray source that is also horizontally invariant, the photon flux depends only on the altitude coordinate z . Therefore, it is possible to efficiently simulate the gamma-ray flux at the observation altitude by using a fictitious detector occupying an entire horizontal slice. Then, this flux can then be injected in a realistic detector simulation (Baldoncini et al. [18]). However, in practice, assumptions of a flat geometry or a homogeneous source may be too strong (see e.g. Satoh et al. [19]), requiring alternative approaches.

Some authors have proposed mixed models that combine a Monte Carlo simulation in the vicinity of the detector with deterministic models of photon transport beyond the detector (Smith et al. [20], Shaver et al. [21]). These deterministic models are based on the resolution of a simplified radiative transfer equation.

Another approach to address the Monte Carlo inefficiency problem is to rely on Importance Sampling (IS) methods. In particular, an efficient strategy is to reverse the simulation of gamma-rays trajectories, starting from the detector until incidentally reaching a source, as sketched in figure 1. This is the approach adopted in this work. This method guarantees that all simulated trajectories arrive at the detector, by con-

struction. However, it does not ensure that a backwards generated trajectory starts from a source of gamma-rays. Nonetheless, when the source region is significantly larger than the detector one, impressive improvements in simulation efficiency are obtained.

However, achieving accurate backward Monte Carlo transport requires dedicated algorithms and software developments that are technically more complex than forward methods. Moreover, these functionalities are typically added to existing forward Monte Carlo software, not initially designed for running backwards, which further complicates the task (see e.g. Gabler et al. [22], Pourrouquet et al. [23], Robinson et al. [24], Malins et al. [25], and Desorgher et al. [26] in the case of GEANT4). Not all of these (modified) software are publicly available. Furthermore, when available, comparisons to forward results show significant discrepancies (see e.g. Desorgher et al. [26], Looper [27], Jun et al. [28]).

In addition, gamma-ray sources have a discrete emission spectrum, while existing backwards going algorithms are typically designed to sample continuous spectra. In the latter case, the stopping condition is determined solely by the position of the particle, based on the geometry of the simulation, rather than its energy. Thus, the final energy of a backwards generated trajectory is unlikely to match any of the source emission lines. As a result, commonly available backward Monte Carlo implementations, such as the one used in GEANT4, are not suitable for our transport problem.

Recently, new techniques for backward transport have been developed (Niess et al. [29]), which efficiently account for the scattering of low-energy muons in muography problems, with an accuracy comparable to forward methods (see e.g. Niess [30]). These techniques are applied to gamma-ray transport, which is discussed in section 3. Additionally, we propose a simple modification to the backwards going algorithm that enables sampling of discrete emission lines. The modified algorithm has been implemented in a new software library called GOUPIL (**G**amma transp**Or**t **U**tility, a**P**roximate but revers**Ib**Le), which is dedicated to transporting gamma-rays emitted by radionuclides. The presentation and validation of this library are discussed in the rest of the paper, specifically in sections 4 and 5.

2. Transport and secondaries

The algorithmic developments presented in this article were motivated by the need to accelerate the atmospheric transport of gamma photons produced by natural radioactivity in the air and soil. Radioactivity in the air comes mainly from the short-lived daughters of ^{222}Rn , such as ^{214}Pb and ^{214}Bi . In the soil, it results from the decay chains of Uranium (^{235}U , ^{238}U) and Thorium (^{232}Th), as well as from the decay of ^{40}K . These isotopes and their progenies are contained in rocks. Therefore, a gamma photon detected at a particular observation point is likely to originate from all directions in space. That is, the gamma photon sources analysed in this study are diffuse in nature.

Furthermore, these sources exhibit a gamma emission spectrum that encompasses various lines corresponding to the transition energies between the different energy levels of the radionuclides in question. For all applications of the methods presented, we use a simplified emission spectrum corresponding to the primary emission lines accompanying the $^{214}\text{Pb} \rightarrow ^{214}\text{Bi}$ and $^{214}\text{Bi} \rightarrow ^{214}\text{Po}$ decays (see table 1). These radionuclides are found both in the atmosphere and in the soil and cover an energy range representing the gamma photons produced by natural and artificial radioactivity. Nonetheless, the methods described below can also be applied to other emission spectra.

Table 1: Main gamma emission lines in the ^{222}Rn decay chain, according to [31]. Reported intensities are relative to the corresponding decay activity. Only emission lines with an intensity greater than 3% are considered.

Decay	Energy (MeV)	Intensity (%)
$^{214}\text{Pb} \rightarrow ^{214}\text{Bi}$	0.242	7.3
	0.295	18.4
	0.352	35.6
$^{214}\text{Bi} \rightarrow ^{214}\text{Po}$	0.609	45.5
	0.768	4.9
	0.934	3.1
	1.120	14.9
	1.238	5.8
	1.378	4.0
	1.764	15.3
	2.204	4.9

Figure 2 displays the cross-sections of the various interaction mechanisms between a gamma photon and air molecules. Gamma photons lose their energy primarily through Compton collisions, which are dominant at emission energies. Eventually, photons are absorbed by the photoelectric effect when their energy decreases to less than a hundred keV. These processes release a secondary electron that can also propagate. In addition, for energies greater than $2m_e \simeq 1$ MeV (where m_e is the mass of the electron), photons can be converted into an e^+e^- pair within the electromagnetic field of medium's atoms (pair production). Moreover, gamma-rays may be emitted by secondary electrons and positrons through braking radiation (bremsstrahlung) or electron-positron annihilation. To determine the total flux of particles that ultimately reach the detector, one should in principle consider the entire chain of interactions, including primary and secondary particles.

To quantify the secondary flux, we conducted a synthetic experiment using GEANT4 (version 10.7.4, `G4EmStandardPhysics`). We used an isotropic and homogeneous propagation medium filled with dry air of density 1.205 mg/cm^3 , which corresponds to temperature conditions of 20°C under 1 bar of atmospheric pressure. A point source of gamma-rays is placed in this medium, which is isotropic in direction and has an emission spectrum consistent with the progeny of ^{222}Rn , according to table 1. The experiment is to count the outgoing particles through a fictitious sphere of radius r centred on the source.

Figure 3 shows the results obtained at different distances, r , from the source. The outgoing flux is composed of less than 1% secondary particles. This is due to the fact that electrons are less penetrating than photons, and that the probability of emitting a secondary gamma photon is low, at these energies. Therefore, secondary particles have a minimal contribution to the transport. However, secondary particles account for 96% of the CPU computing time.

Therefore, we will only transport primary photons in order to improve computational efficiency (which results in a slight underestimation of gamma-ray fluxes, up to one

percent). In addition, this approximation significantly simplifies the backward transport, discussed hereafter. Nonetheless, it is important to remember that secondary particles are crucial in simulating detector response, as they are responsible for depositing energy in sensitive materials. Neglecting them is only possible at a sufficient distance from the detector's sensitive zones. What constitutes a sufficient distance depends on the application and the desired accuracy. The particular case of a scintillation detector is discussed in the validation section (sec. 5.2).

3. Transport algorithms

The details of the Monte Carlo transport of gamma-rays are discussed below. For the sake of clarity, we will first consider a simple setup that captures the essence of the problem. We will then present a forward transport algorithm and its inversion. Finally, we will discuss the generalisation to more realistic setups.

3.1. Problem formulation

A set of gamma-ray sources is assumed to be distributed within a closed propagation medium bounded by an external contour \mathcal{E} . Inside this medium, a second closed volume containing the detector is isolated. The contour of this second volume is called the collection surface, \mathcal{C} . In addition, it is assumed that there are no sources below \mathcal{C} . The Monte Carlo transport amounts to generating a set of trajectories from the sources to a point in \mathcal{C} , without intersecting \mathcal{E} , and according to the laws of physics. The set of these trajectories is denoted T . It is further required that T -trajectories intersect \mathcal{C} exactly once, at the end. This condition will become useful when the problem is generalised in section 3.4. For the time being, note that it amounts to stopping the simulation as soon as a trajectory intersects with \mathcal{C} .

The trajectory of a Monte Carlo photon consists in a sequence of n collision vertices connected by straight-line segments, as illustrated in figure 4 below. In addition, the trajectory includes an incoming segment from the source to the first collision and an outgoing segment from the last collision to the collection surface. The positions of the collision vertices are denoted as \mathbf{r}_i with $i \in [1, n]$, and by extension $\mathbf{r}_0 = \mathbf{r}_I$ ($\mathbf{r}_{n+1} = \mathbf{r}_F$) represents the starting (arrival) point of the trajectory. The photon momentum at the exit of \mathbf{r}_i is denoted $\mathbf{k}_i = \nu_i \mathbf{u}_i$, where ν_i is the photon energy and \mathbf{u}_i a unit vector representing its momentum direction. Note that the momentum remains constant along a segment, e.g. between two collisions. Thus, a Monte Carlo trajectory is represented by an ordered set of states, $S_i = \{\nu_i, \mathbf{r}_i, \mathbf{u}_i\}$.

It is assumed that the propagation medium has a spatially uniform composition, but a potentially variable density ρ , e.g. representing the Earth's atmosphere. Therefore, the atomic cross-section σ , for photons interactions with atoms of the propagation medium, depends solely on ν , not on \mathbf{r} , nor on \mathbf{u} . However, the mean free path of photons depends on the density ρ of the medium, and therefore on \mathbf{r} , as

$$\frac{1}{\lambda(\nu, \mathbf{r})} = \rho(\mathbf{r}) \frac{\mathcal{N}_A}{M} \sigma(\nu), \quad (1)$$

where M represents the molar mass of the propagation medium, which is constant based on our assumptions. Thus, in some circumstances it is relevant to instead consider the

mean free path in units of grammage, defined as

$$\Lambda(\nu) = \rho\lambda, \quad (2)$$

which only depends on ν .

To account for the amount of target material between two vertices in a medium of variable density, let us define the grammage function $X(d; \mathbf{r}, \mathbf{u})$, as

$$X(d; \mathbf{r}, \mathbf{u}) = \int_0^d \rho(\mathbf{r} + s\mathbf{u}) ds, \quad (3)$$

where d represents the distance travelled from \mathbf{r} along the line of sight \mathbf{u} . We denote $d_i = \|\mathbf{r}_i - \mathbf{r}_{i-1}\|$ the distance between vertices $i-1$ and i , and $X_i = X(d_i; \mathbf{r}_{i-1}, \mathbf{u}_{i-1})$ the column depth (grammage) between these same vertices. Note that for $\rho > 0$, the grammage function is always monotonically increasing according to d , making it invertible given \mathbf{r} and \mathbf{u} .

The survival probability of a photon between vertices i and $i+1$ depends on X_i as

$$P_{s,i} = e^{-\ell_i}, \quad \ell_i = \frac{X_i}{\Lambda(\nu_{i-1})}. \quad (4)$$

The corresponding Probability Density Function (PDF) of interacting at the distance d_i from \mathbf{r}_{i-1} is

$$p_{s,i} = \frac{P_{s,i}}{\lambda(\nu_{i-1}, \mathbf{r}_i)}. \quad (5)$$

At a collision vertex, the energy of the photon changes discontinuously from ν_{i-1} to ν_i , and its direction changes from \mathbf{u}_{i-1} to \mathbf{u}_i . To account for the different dynamics of photon interaction processes, let us write the corresponding collision PDF as a mixture density, as

$$\begin{aligned} p_c(\nu_i, \mathbf{u}_i; \nu_{i-1}, \mathbf{u}_{i-1}) &= \sum_j q_j(\nu_i; \nu_{i-1}) p_{c,j}(\nu_i, \mathbf{u}_i; \nu_{i-1}, \mathbf{u}_{i-1}), \\ q_j(\nu_i; \nu_{i-1}) &= \frac{\sigma_j(\nu_{i-1})}{\sigma(\nu_{i-1})}, \\ p_{c,j}(\nu_i, \mathbf{u}_i; \nu_{i-1}, \mathbf{u}_{i-1}) &= \frac{1}{\sigma_j(\nu_{i-1})} \frac{\partial^2 \sigma_j}{\partial \nu_i \partial \Omega_i}, \end{aligned} \quad (6)$$

where Ω_i represents the solid angle at which the photon emerges during a collision. The index j runs over interaction processes, such that $\sigma = \sum \sigma_j$. The details of these processes, such as their cross-sections, are not relevant at this point, and will be discussed in section 4.2.

A Monte Carlo trajectory is characterised by a sequence of states, \mathbf{S} , resulting from a succession of statistically independent random events, as follows: first, interacting at the point \mathbf{r}_i (event of density $p_{s,i}$, eq. 5); then, resolving this interaction (event of density p_c , eq. 6); and so on. The PDF $p(\mathbf{S})$ of a trajectory corresponding to this succession of events is important for the rest of the discussion. This PDF can be expressed from the previous definitions. Note that the last step of the trajectory, intercepting the collection surface, differs from the others. In this case, it is sufficient to consider the survival probability

$P_{s,n+1}$ of the photon between vertices n and $n+1$ (eq. 4). After a few simplifications, $p(\mathbf{S})$ writes

$$p(\mathbf{S}) = P_s(\mathbf{S})c(\mathbf{S}), \quad c(\mathbf{S}) = \prod_{i=1}^n \frac{p_{c,\mathbf{j}(i)}(\nu_i, \mathbf{u}_i; \nu_{i-1}, \mathbf{u}_{i-1})}{\lambda_{\mathbf{j}(i)}(\mathbf{r}_i, \nu_{i-1})}, \quad (7)$$

where \mathbf{j} is an index vector indicating the interaction processes for the n collision vertices. The prefactor P_s corresponds to the survival probability of the photon over the entire trajectory, i.e. between the emission point and the collection point. This survival probability writes

$$P_s = \exp\left(-\sum_{i=1}^{n+1} \ell_i\right). \quad (8)$$

Finally, when discussing the following transport algorithms, it is useful to distinguish between three types of interaction processes: absorption ($\nu_{i+1} = 0$), elastic ($\nu_{i+1} = \nu_i$) and inelastic ($\nu_i > \nu_{i+1} > 0$). The corresponding sets of j process indices are denoted as ABSORPTION, ELASTIC, and INELASTIC.

3.2. Forward algorithm

With the previous notations and definitions, we can now discuss the forward algorithm for generating Monte Carlo trajectories, detailed below (alg. 1). This is a classical algorithm (see e.g. Berger [33]). But, we find useful to recall it explicitly for the sake of understanding of the reverse method.

Some steps in algorithm 1 are represented by external functions that are not described herein, for brevity. For instance, the function OPEN01 (L6) consumes a random stream \mathcal{R} and returns a real number that is uniformly distributed over the open interval $(0, 1)$. By using the open interval instead of $[0, 1]$, we escape some numerical issues. Let us also point out that the function CROSSSECTIONS (L2, L23) returns a vector of values that correspond to the cross-sections of the various interaction processes.

The functions DISTANCETOVERTEX (L8) and DISTANCETOINTERFACE (L9) account for the geometry of the propagation medium. The first function inverts the column depth (grammage, X) along the line of sight, \mathbf{u} , to determine the geometric distance d (noted d_V in algorithm 1). In the case of a medium with uniform density, this inversion is straightforward, as $d = X/\rho$. However, in general, this step might be complex, although always solvable for $\rho > 0$, as previously noted. The second function, DISTANCETOINTERFACE, returns the distance to the first intersected interface along a line of sight. This function may be provided by an external ray-tracing algorithm. For the simple setup considered herein, the intersected interface is either the collection surface \mathcal{C} or the external border \mathcal{E} encapsulating the source medium. In the absence of a boundary, function DISTANCETOINTERFACE would return $+\infty$, for example.

The two other functions appearing in algorithm 1 simulate collisions using the random stream \mathcal{R} . Function SELECTPROCESS (L16) is rather simple as it selects one of the interaction processes with probability $q_j = \sigma_j/\sigma$. However, an efficient implementation of function RANDOMISECOLLISION (L20, L22) is more complex, which will be discussed in section 4.

Let us also emphasize some technical properties of algorithm 1. First, this algorithm generates two trajectory topologies, depending on the stop condition (L10 or L17). The first topology, which stops on an interface, contains the T -trajectories of interest. Note

Algorithm 1 Forward Monte Carlo transport.

Require: $\nu_I > 0$, $\|\mathbf{u}_I\| = 1$, \mathcal{R} (a random stream).

```
1:  $(\nu, \mathbf{r}, \mathbf{u}) \leftarrow (\nu_I, \mathbf{r}_I, \mathbf{u}_I)$  ▷ Initialisation to source parameters.
2:  $\boldsymbol{\sigma} \leftarrow \text{CROSSSECTIONS}(\nu)$ 
3:  $\sigma \leftarrow \text{SUM}(\boldsymbol{\sigma})$ 
4: loop
5:    $\Lambda \leftarrow \frac{M}{N_A \sigma}$ 
6:    $\zeta \leftarrow \text{OPEN01}(\mathcal{R})$ 
7:    $X \leftarrow -\Lambda \ln \zeta$ 
8:    $d_V \leftarrow \text{DISTANCETOVERTEX}(\mathbf{r}, \mathbf{u}, X)$ 
9:    $d_I \leftarrow \text{DISTANCETOINTERFACE}(\mathbf{r}, \mathbf{u})$ 
10:  if  $d_I < d_V$  then ▷ Stop on an interface.
11:     $\mathbf{r} \leftarrow \mathbf{r} + d_I \mathbf{u}$ 
12:    return  $(\nu, \mathbf{r}, \mathbf{u})$ 
13:  else
14:     $\mathbf{r} \leftarrow \mathbf{r} + d_V \mathbf{u}$ 
15:  end if
16:   $j \leftarrow \text{SELECTPROCESS}(\boldsymbol{\sigma}, \sigma, \mathcal{R})$ 
17:  if  $j \in \text{ABSORPTION}$  then ▷ Stop by absorption.
18:    return  $(0, \mathbf{r}, \mathbf{u})$ 
19:  else if  $j \in \text{ELASTIC}$  then
20:     $(\cdot, \mathbf{u}) \leftarrow \text{RANDOMISECOLLISION}(j, \nu, \mathbf{u}, \mathcal{R})$ 
21:  else
22:     $(\nu, \mathbf{u}) \leftarrow \text{RANDOMISECOLLISION}(j, \nu, \mathbf{u}, \mathcal{R})$ 
23:     $\boldsymbol{\sigma} \leftarrow \text{CROSSSECTIONS}(\nu)$ 
24:     $\sigma \leftarrow \text{SUM}(\boldsymbol{\sigma})$ 
25:  end if
26: end loop
```

that in this topology, we also find trajectories leaving the propagation medium through \mathcal{E} . The second topology contains trajectories that are absorbed before ever reaching an interface.

Secondly, algorithm 1 is analogue, i.e. trajectories are generated according to $p(\mathbf{S})$ (eq. 7). Therefore, in the following we equate *forward* and *analogue*. Note however that, generally speaking, forward Monte Carlo procedures might rely on Importance Sampling methods, contrary to algorithm 1.

3.3. Backward algorithm

As backward Monte Carlo methods are uncommon, we shall first discuss some of their specificities before proceeding with the inversion of the forward procedure (alg. 1).

3.3.1. Backward Monte Carlo methods

A Monte Carlo transport procedure defines a functional relationship between the departure state S_I and the arrival state S_F of a trajectory. This relationship can be expressed as

$$S_F = F(S_I, \mathcal{R}), \tag{9}$$

where \mathcal{R} represents a random stream that is consumed by F . Let us further assume that the functional inverse according to S of F exists, such that

$$S_I = B(S_F, \mathcal{R}). \quad (10)$$

Then, it is important to note that the composition

$$B(\cdot, \mathcal{R}') \circ F(\cdot, \mathcal{R})(S_I) \neq S_I, \quad (11)$$

does not restore the initial state S_I . This is because the outcomes of the B and F transport procedures depend on statistically independent random streams, \mathcal{R}' and \mathcal{R} . That is, backward Monte Carlo transport does not reverse time in the same way as rewinding a film. Instead, the forward and backward procedures both reflect the collision physics, which is inherently stochastic.

It is also interesting to observe that if the forward procedure is analogue, usually the inverse one is not. Indeed, let us denote p_F (p_B) the PDF of producing a trajectory with procedure F (B). Then, for a trajectory \mathbf{S} , we have [29]

$$p_B(\mathbf{S})dS_I = p_F(\mathbf{S})dS_F. \quad (12)$$

Thus, the two procedures cannot be simultaneously analogue, except for unitary processes, e.g. that conserve the particle's energy.

The functional inverse B is a particular case of a backward procedure, which is not necessarily optimal and its existence is not guaranteed either. In practice, one frequently relies on alternative methods, such as an adjoint formulation or the use of approximate processes (see e.g. corollary 1 of Niess et al. [29]). In any case, the physical correctness is restored by weighting backwards simulated trajectories by a factor ω , such that

$$\omega(\mathbf{S})p^*(\mathbf{S}) = p(\mathbf{S}), \quad (13)$$

where p^* denotes the PDF of the backward generation procedure, whether the inversion is functional or not.

Consequently, backward algorithms belong to the family of Importance Sampling (IS) methods. A valid backward algorithm produces any trajectory of interest generated by the forward algorithm (i.e. $p^*(\mathbf{S}) > 0$ for all $\mathbf{S} \in T$), and the corresponding ω weights satisfy to equation 13. The efficiency of the backward method, i.e. Monte Carlo convergence, depends on the distribution of weights ω . It is advisable to achieve a relatively uniform distribution of weights, as a finite number of Monte Carlo samples are used in practice. With that respect, let us point out that in the case of functional inversion, the weights are given by the Jacobian factor $\omega = |d\nu_I/d\nu_F|$, which tends to be $\mathcal{O}(1)$ for non-chaotic systems.

3.3.2. Constrained backward collisions

After these initial comments, let us now consider the inversion of algorithm 1 itself. Essentially, this algorithm can be inverted by applying corollary 3 of Niess et al. [29]. The main difficulty lies in the backward simulation of collisions. With usual methods, the photon's initial energy (ν_{i-1}) is not restricted by the source energy (ν_I), but only by the kinematics of the physical process. To account for this external constraint, a simple

yet efficient solution is to override the energy ν_{i-1} of the incoming photon to ν_I for any collision where $\nu_{i-1} \geq \nu_I$. In addition, a corrective weight must be applied whenever ν_{i-1} is overridden, as

$$\omega(\nu_i, \nu_{i-1}) = \frac{p_c(\nu_i; \nu_{i-1})}{1 - P_c^*(\nu_{i-1}; \nu_i)}, \quad (14)$$

where p_c is the PDF for a forward collision, and P_c^* the Cumulative Distribution Function (CDF) for an unconstrained backward collision. This procedure is essentially similar to stopping a particle as soon as it crosses a boundary surface, but operating on the particle's energy instead of its position. The corresponding algorithm 2 is detailed below, and a proof is provided in [Appendix A](#).

Algorithm 2 Constrained Backward Collision.

Require: $\nu_i \in (0, \nu_I)$, \mathcal{R} (a random stream).

```

1:  $(\nu_{i-1}, \omega_c) = \text{RANDOMISEBACKWARD}(\nu_i, \mathcal{R})$ 
2: if  $\nu_{i-1} < \nu_I$  then
3:   return  $(\nu_{i-1}, \omega_c)$ 
4: else
5:    $p_c \leftarrow \text{PDFFORWARD}(\nu_i, \nu_I)$ 
6:    $P_c^* \leftarrow \text{CDFBACKWARD}(\nu_I, \nu_i)$ 
7:    $\omega_c \leftarrow \frac{p_c}{1 - P_c^*}$ 
8:   return  $(\nu_I, \omega_c)$ 
9: end if
```

3.3.3. Backward absorption

Another point requiring attention is the backward treatment of absorption processes. Let us recall that, as discussed in section 2, we only consider primary photons. This means that any collision process that does not restore the incident photon is considered as absorbing and terminates the Monte Carlo trajectory. But, in the case of a backward collision, the absorbing processes are undetermined as we do not specify any of the collision's product. Despite this, we cannot disregard them as they alter the survival probability P_s of T -trajectories, which appears in equation 7 and gives p .

One possible solution is to treat absorption as a continuous process, as demonstrated in [Appendix B](#). Let Λ_a be the mean free path of the absorption processes only. During trajectory randomisation, absorption processes are disregarded, but they are taken into account with an additional weight of $\omega_a = P_s[\Lambda_a]$, which corresponds to the trajectory survival probability according to the absorption processes alone (i.e. [eq. 4](#), but with Λ_a substituted for Λ).

A more subtle alternative is to modify the PDF of backwards generated trajectories by a factor of $P_s[\Lambda_a] \in [0, 1]$, instead of modifying their weights. This can be achieved by randomly eliminating backward trajectories with a probability of $r = 1 - P_s[\Lambda_a]$ using a Russian Roulette method. Moreover, doing this step-by-step, between two successive vertices, avoids unnecessary resource wastage in generating full trajectories that would eventually be eliminated. Section 3.3.5 hereafter presents a complete backward algorithm using the latter method.

3.3.4. Backward photo-peaks

Before discussing the complete backward transport, we shall consider the particular case of photo-peak trajectories. These events are elastic, meaning that the photon energy, $\nu = \nu_I$, is conserved over the entire trajectory. However, the photon may still undergo elastic collisions, such as Rayleigh scattering. As elastic collisions are self-inverse processes (see e.g. Appendix D of Niess et al. [29]), the forward and backward transport of photo-peak events can be made almost identical. The only difference lies in the stopping condition. In the forward case, photo-peak trajectories stop when they intersect the collection surface \mathcal{C} . In the backward case, the forward algorithm 1 can be used (starting from S_F), but the trajectory should be stopped as soon as an inelastic collision would occur (i.e. after L21, before simulating the inelastic collision). The corresponding stop point, \mathbf{r}_I , is selected as a potential source location for the backward trajectory. Furthermore, the backward trajectory should be weighted by a factor

$$\omega = \lambda_{\text{in}}(\mathbf{r}_I, \nu_I), \quad (15)$$

where λ_{in} represents the mean free path for inelastic processes only, excluding absorbing and elastic processes. A proof of this method is provided in Appendix C. Note that this approach considers absorption processes as self-inverses, which is consistent with the previous discussion (sec. 3.3.3).

3.3.5. Complete backward algorithm

Using the constrained backward collision procedure, RANDOMISECONSTRAINED, as previously stipulated by algorithm 2, we can invert algorithm 1. Applying corollary 3 of Niess et al. [29], in the absence of any continuous process, leads to the algorithm 3 below, where the weight ω_c (L29, L33) corresponds to the term $|\partial\epsilon_{j+1}/\partial\epsilon_j|\omega_b$ of [29, eq. 15] (using the original notations). However, note that T -trajectories are terminated by the condition of line L22 instead of an interface crossing. This corresponds to the specific case of photo-peaks transport, which was discussed previously in section 3.3.4. The stopping condition is reached either by setting $\nu_F = \nu_I$ from the beginning or when an inelastic collision triggers the energy constraint ν_I .

Let us point out that the sampling of the interaction process (L17) uses the same physical cross-sections as in the forward case, due to Lemma 5 of [29]. This enables the use of the same backward absorption process as in the forward case. However, Lemma 5 requires $\sigma_j > 0$ for all j , which is not verified in this case for the production of an e^+e^- pair. This is kinematically forbidden for $\nu < 2m_e$. One possible solution is to group this process with the photoelectric interaction. Both processes are of absorption type and therefore identical from the point of view of the transport algorithm. This approach ensures that the total cross-section of the absorption processes verifies $\sigma_a > 0$.

As a cross-check, it is useful to determine the PDF of the T -trajectories generated by algorithm 3. After simplification, we find

$$\begin{aligned} p^*(\mathbf{S}) &= P_s(\mathbf{S})c^*(\mathbf{S}), \\ c^*(\mathbf{S}) &= \frac{1}{\lambda_{\text{in}}(\mathbf{r}_I, \nu_I)} \prod_{i=1}^n \frac{P_{c,j(i)}^*(\nu_{i-1}, \mathbf{u}_{i-1}; \nu_i, \mathbf{u}_i)}{\lambda_{j(i)}(\mathbf{r}_i, \nu_i)}. \end{aligned} \quad (16)$$

The corresponding weight returned by the backward procedure is

$$\omega(\mathbf{S}) = \lambda_{\text{in}}(\mathbf{r}_I, \nu_I) \prod_{i=1}^n \frac{\sigma_{\mathbf{j}(i)}(\nu_i)}{\sigma_{\mathbf{j}(i)}(\nu_{i-1})} \omega_{c, \mathbf{j}(i)}(\nu_{i-1}, \nu_i). \quad (17)$$

By definition, for each collision vertex of index i , we have

$$\frac{\sigma_j(\nu_i)}{\lambda_j(\mathbf{r}_i, \nu_i)} = \frac{\sigma_j(\nu_{i-1})}{\lambda_j(\mathbf{r}_i, \nu_{i-1})}, \quad (18)$$

$$p_j^*(\nu_{i-1}, \mathbf{u}_{i-1}; \nu_i, \mathbf{u}_i) \omega_{c, j}(\nu_{i-1}, \nu_i) = p_j(\nu_i, \mathbf{u}_i; \nu_{i-1}, \mathbf{u}_{i-1}).$$

Thus, it is verified that $p^* \omega = p$, i.e. the weighted backward trajectories yield back the forward PDF as per equation 7.

Note that algorithm 3 generates two additional trajectory topologies, which are not part of T , via the stop condition of line L11 or line L18. The first case corresponds to the intersection of an interface, such as the external border \mathcal{E} . In this case, these trajectories could be associated with an external surface source, such as an external flux of photons, which is not considered here. The second topology represents backwards-absorbed trajectories. These trajectories do not have an equivalent in the forward formulation. They result from the effective treatment of absorption processes, which randomly eliminate some photons to ensure the correct PDF for T-trajectories. If absorption is considered to be continuous, this branch of the algorithm is not reached. However, this leads to additional variability in the weights by a factor of $P_s[\Lambda_a] \leq 1$.

3.4. Generalisation

Let us now generalise the previous algorithms to more complex setup. But, before delving into the details, let us emphasize that the forward (alg. 1) and backward (alg. 3) transport procedures are almost identical. They both use the same functions for the transport between vertices (CROSSSECTIONS, DISTANCETOVERTEX, and DISTANCETOINTERFACE), but with opposite directions. The main difference between the two algorithms is in the treatment of inelastic collisions, which call on distinct functions (and weightings), RANDOMISECOLLISION or RANDOMISECONSTRAINED. Thus, in practice one can implement a single bi-directional procedure that is valid in both cases, adding a few conditional branches. However, for clarity we presented two distinct algorithms in the previous sections.

3.4.1. Realistic setup

For a realistic setup, Monte Carlo trajectories may pass through different media with distinct compositions before reaching the collection surface. For instance, the propagation volume may consist of a soil-air binary with an interface described by topography data. Furthermore, the detector has a composite structure that includes inert mechanical elements in addition to its gamma-ray sensitive area.

In the forward case, a method for simulating trajectories within a complex geometry is to iterate algorithm 1. When encountering an interface (L10) that is not the collection surface \mathcal{C} , instead of terminating the procedure (L12), one restarts from the beginning (L2), after updating the composition of the propagation medium (on which CROSSSECTIONS actually depends). It is important to note that the photon then straddles two

media, which is numerically problematic. Thus, in practice, one notifies this interface crossing for the next call to function `DISTANCETOINTERFACE` to exclude the interface that was just crossed.

In the backward case, let us point out that algorithm 3 applies transport weights at the level of collision vertices. Consequently, the previous method is also valid since the conditions for stopping on and starting from an interface are of *flux* type (see Niess et al. [29, section 2.6]).

Another point is that gamma-ray sources have multiple emission lines, rather than being mono-energetic. In a forward simulation, the initial photon energy is selected with probabilities p_k , according to the respective activities of emission lines. In a reverse simulation, if the p_k are independent of the position \mathbf{r} , the source energy can be pre-selected, similar to a forward simulation. Otherwise, the source energy can be selected based on an a priori distribution, $p_{b,k}$, and then the trajectory shall be weighted a posteriori by the ratio

$$\omega_s = \frac{p_k(\mathbf{r}_I)}{p_{b,k}}. \quad (19)$$

3.4.2. Mixed Monte Carlo

It was previously mentioned that the transport procedure can stop and restart at any interface crossing. This allows for the simulation of a Monte Carlo trajectory to be split into two parts, which presents interesting possibilities. For instance, consider a set of T_0 trajectories generated using the backward procedure described above. If we want to reduce the collection surface to a new interface, \mathcal{C}' , inscribed under the old surface, \mathcal{C} , we can do so by extending the existing T_0 trajectories using a forward procedure. Let us denote T'_0 these extended trajectories.

The T'_0 -trajectories correspond to sources that are external to the volume included in \mathcal{C} . However, it is also likely that the volume between \mathcal{C} and \mathcal{C}' contains sources, which are called *internal*. To complete the picture, T'_0 should be extended with T_1 -trajectories, whose sources are internal. Let us denote by N_0 (N_1) the number of events simulated with an external (internal) source. Also note A_0 (A_1) the total activity of external (internal) sources. The two sets of trajectories, T'_0 and T_1 , can be combined by assigning a weight of

$$\omega_A = \frac{A_i}{N_i}, \quad (20)$$

to each trajectory based on its origin.

Thus, the backward transport procedure reduces a set of sources distributed over a volume external to \mathcal{C} to a surface flux that enters \mathcal{C} . This flux is represented by the states S_F that terminate the trajectories T_0 , weighted according to A_0/N_0 . Therefore, it is advantageous to use two distinct transport algorithms as follows. To begin, a contour \mathcal{C} is defined to surround the sensitive area of the detector. Next, external sources to \mathcal{C} are reduced to an incoming flux using a backward simulation procedure, such as algorithm 3. Finally, a forward simulation of the detector's response to the incoming flux and any internal sources is carried out. The second simulation accounts for the production of secondary particles.

Let us emphasize that the first backward simulation does not require knowledge of the internal geometry of \mathcal{C} . By contrast, the second forward simulation requires both

the internal and external geometry, as a particle may pass through \mathcal{C} multiple times before detection. Note that during the backward simulation, it is necessary to exclude re-entrant trajectories to be consistent with the forward simulation. Therefore, we have imposed that the simulation of trajectories from external sources stops as soon as \mathcal{C} is intersected.

4. Goupil implementation

Let us now discuss the software implementation of the Monte Carlo transport algorithms (sec. 3) within the GOUPIL software library.

4.1. Software architecture

GOUPIL has been implemented in Rust [34]. In our view, Rust is an excellent language for a Monte Carlo transport engine, enabling the creation of dependable software without compromising performances. However, Rust is not yet widely used in the scientific community due to its relatively recent introduction. Therefore, we opted for a more traditional user interface, combining Python and C. That is, the internal *Rusty* nature of GOUPIL should be transparent to end-users.

Thus, GOUPIL is provided as a Python 3 module, generated from the Rust source using PyO3, and available for download from PyPI [35]. The project source is publicly available (under the terms of the LGPL-3.0 license) from GitHub [36]. The module’s functionalities are organised into objects (Python classes) according to a structure that can be consulted online from ReadTheDocs [37]. Time-sensitive routines are vectorised to take full advantage of Rust performances. These routines manipulate `numpy.ndarray` at the Python level. For instance, the `TransportEngine.transport` method receives a vector of initial states (S_I) as input and transforms it, in-place, into a vector of final states (S_F).

In addition, GOUPIL can be used with an external geometry engine. This corresponds to the call to the `DISTANCETOINTERFACE` function in the transport algorithms (alg. 1 and alg. 3). For this purpose, GOUPIL specifies an input interface in C, which is also documented on ReadTheDocs [37]. The external geometry engine is loaded from Rust in the form of a dynamic library, thus avoiding going through Python during a Monte Carlo run. In practice, to implement this approach, a software adaptation layer needs to be developed between GOUPIL and the external geometry engine. For GEANT4, a pre-existing adapter is included with the Python GOUPIL module.

Finally, let us emphasize that GOUPIL is interoperable with CALZONE [38], a GEANT4 Python wrapper that was developed in conjunction with this work in order to facilitate the building of mixed simulations, as described in section 3.4.2. Yet, the two modules can be used fully independently.

4.2. Collisions

The relevant interaction processes for GOUPIL have been outlined in section 2. Let us recall that, in the absence of secondary particles, it is only necessary to consider the interactions between primary photons and matter. Additionally, interactions that do not lead to an outgoing photon are grouped together as *absorption*. Therefore, we will only

be considering three interaction processes: Compton scattering, Rayleigh scattering and absorption (by the photoelectric effect or the creation of an e^+e^- pair).

In section 3, collision vertices were represented as black boxes characterised by their statistical properties, via the PDF $p_{c,j}$ (or $p_{c,j}^*$, in the backward case). However, the treatment of these collisions is not trivial. In practice, collisions represent a potential bottleneck in Monte Carlo transport requiring dedicated optimisations. In the case of forward Monte Carlo, much work was done to have efficient and accurate implementations of collisions. In particular, let us emphasize the work done for the PENELOPE software (see e.g. Baró et al. [39], Salvat [40]), on which GOUPIL is based.

For a backward simulation, only the Compton process needs to be reversed. Rayleigh scattering is of elastic type, and thus self-inverse. Absorption can also be considered invariant under the conditions of algorithm 3, as discussed earlier (sec. 3). Moreover, Compton collisions are the most frequent interaction process at the $\mathcal{O}(1)$ MeV energies of interest. Thus, they deserve a more in-depth discussion hereafter, in section 4.3.

4.2.1. Target materials

Before discussing the specificities of each interaction process, let us highlight some common properties related to the target materials involved in a collision. First, GOUPIL models materials as perfect gases of atoms, which is a usual assumption for collision processes where energy transfers are much larger than the inter-atomic binding energies ($\lesssim 10$ eV).

The atomic elements' properties are predetermined during library initialization, following the Particle Data Group [41] (PDG). Thus, a GOUPIL material is entirely defined by its atomic composition, expressed in terms of molar or mass fractions. The material molar mass M and its cross-section σ_j , for process j , are given as

$$M = \sum_k x_k M_k, \quad \sigma_j = \sum_k x_k \sigma_{jk}, \quad (21)$$

where the index k runs over the constituent atomic elements of the material, and the x_k designate the corresponding molar fractions. Note that the density of the propagation medium, which may vary spatially, is considered by GOUPIL to be a geometric property, and not intrinsic to the target material.

Secondly, it is generally accepted that, where possible, the collisions parameters should be computed in advance of running a Monte Carlo simulation. This leads to the pre-computation of physics tables for each material, which are interpolated during the simulation instead of performing time-consuming calculations on the spot. The material cross-section σ_j that was defined above (eq. 21) is a typical example. This cross-section is dependent on a single variable, the photon energy ν , which may change during a collision. But, To calculate σ_j , a lengthy numerical integration is usually required. Thus, tabulating σ_j saves a significant amount of computing time, at a modest cost in memory.

GOUPIL uses physics tables that depend on a maximum of two variables. We deliberately avoided using tables with more than two variables due to the large memory overhead that it would imply. For tables with one variable, GOUPIL uses a Piecewise Cubic Interpolation with the method of Higham [42], which is both simple and efficient. For tables with two variables, a Piecewise Bilinear Interpolation is used. The tables meshing should also be discussed. GOUPIL uses three types of meshes (x_i) for a variable of interest

x : arithmetic ($x_i - x_{i-1} = \text{cst}$), geometric ($x_i/x_{i-1} = \text{cst}'$), or irregular. In the latter case, a bisection is used to determine an interval for the point of interest ($x \in [x_i, x_{i-1})$).

For the physics of GOUPIL, accurate atomic tables have been previously published, including detailed cross-sections and form factors. One such compilation is the EPDL (Cullen et al. [32]) atomic tables, which are available in ENDF format from the EPICS [43] project. Another option is the XCOM [44] project, which distributes atomic cross-section tables with a precision comparable to EPDL, for GOUPIL use cases, but with more compact meshes. By default, GOUPIL uses XCOM results for cross-sections and EPDL results for form factors. The atomic tables are loaded on demand from a local directory that can be configured by the user. Note that only the absorption and Rayleigh scattering processes use external atomic tables. In the case of Compton scattering, GOUPIL generates its own material tables, as detailed hereafter (sec. 4.3).

4.2.2. Absorption

Simulating the absorption process is straightforward. One simply stops the transport by eliminating the photon. However, determining the cross-section of this process is more involved. The cross-section of photoelectric interactions is piecewise continuous, with the points of discontinuity reflecting the underlying electronic structure. The XCOM tables, which are used by default by GOUPIL, account for this by duplicating discontinuity points, in order to describe the values of the cross-section on either side of the discontinuity. When combining these atomic data to construct the cross-section of a material, σ_j , according to equation 21, all these discontinuities need to be preserved. This is achieved using the procedure detailed in Appendix D.

4.2.3. Rayleigh scattering

Rayleigh scattering corresponds to the interaction of a photon with the static Coulomb field of a target atom ($\gamma Z \rightarrow \gamma Z$), resulting from the coherent superposition of atomic constituents (nucleus and bound electrons). To model this process, GOUPIL uses an approach similar to PENELOPE. The total cross-section is calculated from accurate atomic tables, using the method of Appendix D, as for absorption. However, for the simulation of collisions, Born's [45] Differential Cross-Section (DCS) is used, such that

$$p(\cos \theta; \nu) \propto \frac{1 + \cos^2 \theta}{2} \left| \frac{F(q, Z)}{Z} \right|^2, \quad (22)$$

$$q^2 = 2\nu(1 - \cos \theta),$$

where $\cos \theta = \mathbf{u}_i \cdot \mathbf{u}_{i-1}$ is the angle between the incident photon and the outgoing photon, and where $F(q, Z)$ is the atomic form-factor, which depends on the momentum $q = \|\mathbf{k}_i - \mathbf{k}_{i-1}\|$ transferred during the collision. Thus, the anomalous scattering term is neglected when simulating the dynamic of the collision, but it is included in the total Rayleigh cross-section.

The scattering angle θ in a Rayleigh collision is sampled using algorithm 5, detailed in Appendix E. This algorithm differs from PENELOPE implementation by balancing memory over CPU usage, since Rayleigh collisions are rare in GOUPIL use cases.

4.3. Compton scattering

Compton scattering corresponds to the interaction between an incident photon and an individual electron in an atom (i.e. $\gamma e^- \rightarrow \gamma e^-$). Klein and Nishina [46] first made a precise prediction of the cross-section of this process, for a free electron, within the framework of quantum electrodynamics. This result is also applicable, to a good approximation, for the bound electrons of an atom when the incident photons are sufficiently energetic. However, when the energy is below $\nu \lesssim 0.1 \text{ MeV}$, it is necessary to consider the electronic structure of the target atom. In the context of a Monte Carlo transport engine, performing a detailed structure calculation would not be affordable. Therefore, GOUPIL relies on an effective model detailed below.

4.3.1. Forward case

Following Baró et al. [47] (see also Ribberfors and Berggren [48]), the cross-section for Compton scattering, differential with respect to the scattering angle θ_i , can be factored as

$$\frac{d\sigma}{d\cos\theta_i} = \pi r_e^2 \left(\frac{\nu_c}{\nu_{i-1}} \right)^2 M(\nu_{i-1}, \nu_c) S(\nu_{i-1}, \cos\theta_i), \quad (23)$$

where M is the matrix element of the interaction with a free electron, such that

$$M(\nu_{i-1}, \nu_i) = \frac{\nu_{i-1}}{\nu_i} + \frac{\nu_i}{\nu_{i-1}} + \left(\frac{m_e}{\nu_i} - \frac{m_e}{\nu_{i-1}} - 1 \right)^2 - 1, \quad (24)$$

and where S is a scattering function, which encodes the electronic structure of the target atom. In previous equation 23, $\nu_c(\cos\theta_i; \nu_{i-1})$ stands for the energy of the outgoing photon in a collision with an electron at rest, solution for ν_i of

$$\frac{m_e}{\nu_{i-1}} - \frac{m_e}{\nu_i} + \cos\theta_i - 1 = 0, \quad (25)$$

which arises from the conservation of energy-momentum.

Baró et al. [47] proposed a parametric model for the scattering function $S(\nu_{i-1}, \cos\theta_i)$, which is accurate without requiring detailed tabulation of S . But, unfortunately, equation 23 is not suitable for inversion, because it is differential according to $\cos\theta_i$ instead of ν_i . Thus, GOUPIL simplifies equation 23, as follow. As an approximation, let us substitute $\theta_C(\nu_i; \nu_{i-1})$ for θ in equation 23, where θ_C is the Compton scattering angle for free electrons, i.e. the solution for θ_i of equation 25. The resulting simplified cross-section, differential according to the energy ν_i of the outgoing photon, writes

$$\frac{d\sigma}{d\nu_i} = \pi r_e^2 \frac{m_e}{\nu_{i-1}^2} M(\nu_{i-1}, \nu_i) S_\nu(\nu_{i-1}, \nu_i), \quad (26)$$

where $S_\nu(\nu_{i-1}, \nu_i) = S(\nu_i, \cos\theta_c(\nu_i; \nu_{i-1}))$ is set. For the scattering function of Baró et al. [47], we obtain

$$S_\nu(\nu_{i-1}, \nu_i) = \sum_k f_k \Theta(\nu_{i-1} - U_k) n_k \circ p_k(\nu_{i-1}, \nu_i), \quad (27)$$

with

$$n_k(p) = \begin{cases} z(-p), & \text{if } p \leq 0 \\ 1 - z(p), & \text{otherwise} \end{cases}, \quad z(p) = \frac{1}{2} \exp\left(\frac{1}{2} - \frac{(1 + 2J_k p)^2}{2}\right), \quad (28)$$

$$p_k(\nu_{i-1}, \nu_i) = m_e \frac{E_k^2 - \nu_i U_k}{\sqrt{2m_e E_k^2 + \nu_i U_k^2}}, \quad E_k^2 = (\nu_{i-1} - U_k)(\nu_{i-1} - \nu_i),$$

where the index k runs on the occupied levels of the atom. The parameters f_k and U_k correspond to the number of occupied levels and the binding energy, respectively. Parameter J_k reflects the inverse of the average momentum of electrons within their orbitals. GOUPIL utilises the PENELOPE values for these parameters (file `pdatconf.p14`), which are dependent on the atomic number Z of the target element.

By construction, GOUPIL model reproduces the total cross-section of Baró et al. [47] as well as the angular distribution, $d\sigma/d\cos\theta$. However, the energy ν_i of the emerging photon is bounded to $\nu_i \in [\nu_{\min}, \nu_{\max}]$, just as in a collision with an electron at rest, where

$$\nu_{\min}(\nu_{i-1}) = \frac{m_e \nu_{i-1}}{m_e + 2\nu_{i-1}}, \quad \nu_{\max}(\nu_{i-1}) = \nu_{i-1}. \quad (29)$$

GOUPIL model does not properly account for energy deposition for incident photons of energy $\nu_{i-1} \lesssim 10$ keV. But, at these energies, the mean free path of photons is largely dominated by photoelectric absorption (see e.g. [fig. 2](#)).

By default, GOUPIL uses a rejection sampling method in order to sample Compton collisions, as detailed in [Appendix F](#). Alternatively, the inverse transform method can also be used, at the cost of a significant increase in memory usage for a moderate CPU gain.

4.3.2. Backwards case

In the backward case, by default, GOUPIL uses an adjoint Compton model. The DCS of the adjoint process is defined over the support $[\nu_{\min}^*, \nu_{\max}^*]$, as

$$\frac{d\sigma^*}{d\nu_{i-1}} = g(\nu_{i-1}, \nu_i) \frac{d\sigma}{d\nu_i}, \quad (30)$$

where σ represents the DCS of the forward processes ([eq. 26](#)), and where

$$\nu_{\min}^*(\nu_i) = \nu_i, \quad \nu_{\max}^*(\nu_i) = \begin{cases} \frac{m_e \nu_i}{m_e - 2\nu_i}, & \text{if } \nu_i < m_e/2 \\ +\infty, & \text{otherwise} \end{cases}. \quad (31)$$

The function g is a regularisation term that ensures the convergence of the total adjoint cross-section, σ^* . The choice $g = \nu_i/\nu_{i-1}$ is adequate, and in practice it yields satisfactory results. The corresponding Monte Carlo weight is

$$\omega_c = \frac{\nu_{i-1}}{\nu_i} \frac{\sigma^*(\nu_i)}{\sigma(\nu_{i-1})}. \quad (32)$$

As in the forward case, by default adjoint Compton collisions are simulated using a rejection method (see [Appendix G](#)).

Alternatively, since GOUPIL Compton model is invertible as per ν_i , backward Compton collisions can also be simulated using the functional inverse, as detailed in [Appendix H](#). However, this approach implies generating large tables of quantiles. Therefore, it is not used by default.

Another point to consider is the inclusion of an external energy constraint, ν_I , during the backward simulation of a Compton collision. Algorithm 2 requires the forward PDF $p_c(\nu_i; \nu_I)$ (L5) and the backward CDF $P_c^*(\nu_I; \nu_i)$ (L6) when the constraint is reached. The former p_c is calculated on the spot by GOUPIL. In practice, the CPU impact is acceptable in this case as the constraint is not frequently reached. However, in the latter case, it is necessary to tabulate P_c^* beforehand. A 1D tabulation per emission line would suffice. But, GOUPIL instead pre-computes a detailed 2D table based on (ν_I, ν_i) . This allows the user to seamlessly modify the value of the external energy constraint, i.e. emission lines.

4.4. Monte Carlo geometry

GOUPIL represents the Monte Carlo geometry as a succession of sectors with uniform atomic composition but variable density. Determining the actual distances between sectors (DISTANCETOINTERFACE) is only partially managed by GOUPIL. For stratified geometries that can be represented using one or more Digital Elevation Model (DEM), GOUPIL disposes of a built-in implementation of the TURTLE algorithm, which was previously described in Niess et al. [49]. See e.g. GOUPIL online documentation [37] for practical examples of usage. For other use cases, an external geometry engine can be used, as mentioned previously in section 4.1.

GOUPIL implements two density models. The first model is a uniform density, while the second model is an exponential density gradient. The latter is typically used to represent the density within a layer of the atmosphere. This model is characterised by an axis \mathbf{n}_ρ and an attenuation length λ_ρ . The density ρ at a point \mathbf{r} is expressed as

$$\rho(\mathbf{r}) = \rho_0 \exp\left(\frac{(\mathbf{r} - \mathbf{r}_0) \cdot \mathbf{n}_\rho}{\lambda_\rho}\right), \quad (33)$$

where ρ_0 is the density in a reference plane containing the point \mathbf{r}_0 . The corresponding grammage function writes

$$X(d; \mathbf{r}, \mathbf{u}) = \begin{cases} \lambda' \left(\exp\left(\frac{d}{\lambda'}\right) - 1 \right) \rho(\mathbf{r}) & \text{if } \mathbf{u} \cdot \mathbf{n}_\rho \neq 0 \\ d\rho(\mathbf{r}) & \text{otherwise} \end{cases}, \quad (34)$$

where

$$\frac{1}{\lambda'} = \frac{\mathbf{u} \cdot \mathbf{n}_\rho}{\lambda_\rho}. \quad (35)$$

This grammage is trivially invertible according to d , for fixed \mathbf{r} and \mathbf{u} , where the inverse corresponds to the DISTANCETOVERTEX function of the transport algorithms.

5. Validation and performances

GOUPIL has undergone various validation tests, two of which are presented below (available from the source, under the `examples/geant4` and `examples/mixed` folders).

The corresponding simulations were conducted on the HPC2 computing grid located at the Clermont-Auvergne [50] mesocentre. The grid has a heterogeneous structure, primarily consisting of Intel Xeon compute nodes running at speeds between 2 and 2.6 GHz.

5.1. Test 1

The first test involves implementing a simulation in GEANT4 and exporting the geometry to GOUPIL using its C interface. The results obtained with both transport engines are then compared.

5.1.1. Test 1 description

To compare GEANT4 and GOUPIL, a simple geometry (illustrated in figure 5) is considered. The simulation volume consists of two boxes superimposed along the (Oz) axis, representing the atmosphere (air) and the soil (rock). These boxes have a square base of $2 \times 2 \text{ km}^2$ along the (Ox) and (Oy) axes. They are filled with `G4_AIR` (1.205 mg/cm^3) and `G4_CARBONATE_CALCIUM` (limestone soil, 2.8 g/cm^3) respectively (materials from the GEANT4-NIST database).

The detector is modelled as a box also with a square base, measuring $20 \times 20 \text{ m}^2$, and 10 m in height. It is placed at the centre of the simulation volume, 5 cm above the soil. The dimensions of the detector in the simulation are significantly larger than those of a gamma-ray spectrometer, which is typically only ten centimetres. However, to compare simulation results, a sufficient number of photons must be collected. This is challenging CPU-wise with a realistic target size, in a forward simulation. Therefore, we have artificially increased the extent of the collection volume.

The gamma-ray sources are uniformly distributed throughout the air volume, excluding the collection volume. Their total activity has been set at $4 \cdot 10^{10} \text{ Bq}$ (corresponding to a volume activity of 10 Bq/m^3 of air). The emission lines of these sources are provided in table 1. The synthetic experiment consist in counting the photons collected on the surface \mathcal{C} that surrounds the detector box.

5.1.2. Comparison of performances

Table 2 provides a summary of the Monte Carlo data generated on the HPC2 grid, as well as the respective performances of the GEANT4 (version 11.4.1), GOUPIL forward and GOUPIL backward simulations. For GEANT4, we used Penelope physics (`G4EMPenelopePhysics`) because it is similar in principle to GOUPIL. However, this choice of physics leads to simulation times 4.3 times longer than with the standard physics of GEANT4 (`G4EmStandardPhysics`). Note that during the GEANT4 simulation, we track all secondary particles to check their contribution to the total flux, as discussed previously (sec. 2). Deactivating the tracking of these secondary particles makes the GEANT4 simulation 20 times faster. Consequently, in the absence of secondary transport and with its standard physics, GEANT4 and GOUPIL forward have comparable CPU performances.

Considering the time Δt_1 required for collecting a photon (see table 2), GOUPIL backward is $\sim 5 \cdot 10^4$ times faster than GOUPIL forward. This impressive gain essentially results from an increase in the Monte Carlo efficiency, ϵ . In a forward simulation, only 3 gamma-rays out of 100 000 generated reach the collection surface \mathcal{C} (which is 20 m large). During a backward simulation, 39 % (33 %) trajectories are compatible with a source located in the atmosphere (soil), 24 % are backwards-absorbed, and the remaining 4 % are invalid trajectories because they turn back towards \mathcal{C} .

Table 2: Statistics of Test 1 Monte Carlo simulations conducted on the HPC2 computing grid of the Clermont-Auvergne mesocentre. The table indicates the number of generated events N , the Monte Carlo efficiency ϵ (i.e. the ratio of the number of gamma-rays collected on \mathcal{C} to the number generated), the average simulation time Δt_0 per generated event, and the average time $\Delta t_1 = \Delta t_0/\epsilon$ per collected gamma-ray. Version 11.2.1 of GEANT4 was used with `G4EMPenelopePhysics`. Note that contrary to GOUPIL, GEANT4 simulations include secondary particles.

Simulation	N	ϵ	Δt_0	Δt_1
GEANT4	$1.5 \cdot 10^{10}$	$3.0 \cdot 10^{-5}$	1.7 ms	56.6 s
GOUPIL (forward)	$1.0 \cdot 10^{11}$	$3.0 \cdot 10^{-5}$	$19.9 \mu\text{s}$	0.67 s
GOUPIL (backward)	$2.0 \cdot 10^9$	$3.9 \cdot 10^{-1}$	$5.8 \mu\text{s}$	$14.9 \mu\text{s}$

Let us point out that GOUPIL has also been tested with realistic ground topographies described by DEMs containing approximately one million nodes, instead of the simple geometry used for comparison with Geant4. In these cases, GOUPIL maintains excellent performance in backward mode by using a `StratifiedGeometry` object (sec. 4.4), which implements Turtle’s ray-tracing algorithm (Niess et al. [49]).

5.1.3. Comparison of results

Let us finally compare the simulations results, particularly concerning the energy spectrum of photons collected on \mathcal{C} . This spectrum is in the form

$$\phi(\nu) = B(\nu) + \sum_{k=1}^n R_k \delta(\nu - \nu_k), \quad (36)$$

where B is a piecewise continuous function (over the intervals $[\nu_k, \nu_{k+1}]$) representing the background of scattered photons, and where the right-hand sum runs over the $n = 11$ emission lines of energies ν_k , resulting in photo-peaks of amplitudes R_k .

Figure 6 shows the results obtained for the background component B . The spectra obtained with GOUPIL forward or backward are consistent. The total background obtained in both cases agrees within 1.5σ , with an uncertainty of 0.4 % on the difference. Similarly, the results obtained with GEANT4 are in excellent agreement with GOUPIL (0.4σ with respect to the backward mode) when considering only primary photons. Secondary particles (γ , e^- , e^+) represent less than 1 % of the total background flux, which is consistent with the results presented previously in section 2.

In addition, figure 7 shows the distribution of the deflection angle (w.r.t. the emission direction) for the background component. As for the energy spectrum, no significant differences are observed between the various simulations.

Table 3 lists the values for the photo-peak intensities, R_k , estimated from a weighted average of all simulation results (GEANT4, GOUPIL forward and backward). Figure 8 shows the relative differences to GOUPIL backward for photo-peaks. As for the background component, forward simulations results (GEANT4, GOUPIL) are consistent with backward ones, considering Monte Carlo uncertainties. Moreover, relative deviations between GOUPIL forward and backward are within 1 %, which aligns with our accuracy objectives.

Table 3: Photo-peak intensities (R_k) in the energy spectrum of gamma-rays collected on the inner surface (\mathcal{C}) of the Test 1 geometry. Reported results are the weighted average of the GEANT4, GOUPI forward and GOUPI backward simulations. Monte Carlo uncertainties on the weighted average are also indicated.

Energy, ν_k (MeV)	Intensity, R_k (kHz)
0.242	7.41 ($\pm 0.3\%$)
0.295	19.94 ($\pm 0.2\%$)
0.352	41.03 ($\pm 0.1\%$)
0.609	64.76 ($\pm 0.1\%$)
0.768	7.70 ($\pm 0.3\%$)
0.934	5.31 ($\pm 0.4\%$)
1.120	27.78 ($\pm 0.2\%$)
1.238	11.34 ($\pm 0.3\%$)
1.378	8.24 ($\pm 0.4\%$)
1.764	35.65 ($\pm 0.2\%$)
2.204	12.77 ($\pm 0.4\%$)

5.2. Test 2

The second test consists in simulating the response of a scintillation-based gamma-ray detector to radio-isotopes scattered within its surrounding environment. This test illustrates the mixed simulation scheme discussed in section 3.4.2, using GOUPI in backward mode to simulate the gamma-ray flux in the vicinity of the detector, and then using GEANT4 to simulate the detector response to this flux. The results of the mixed simulation are compared with an end-to-end GEANT4 forward simulation.

5.2.1. Test 2 description

The gamma-ray detector is a 7.6 cm \times 7.6 cm cylindrical NaI(Tl) detector, modelled following Duc Tam et al. [51] (using the manufacturer settings, provided by table 1). The detector is immersed directly in water, with the omission of any readout electronics, power supply, and waterproof container. While this may not be realistic, these additional elements are not relevant for the present synthetic test. The detector is immersed in a dense medium, rather than air, to ensure the end-to-end forward simulation is CPU-viable on the HPC2 grid.

The source radio-isotopes are distributed uniformly over a 1 m radius sphere centered on the NaI(Tl) scintillator volume, restricted to the water volume (i.e. excluding the detector elements). The source emission lines are taken from Table 1 with a unit volume activity of $\mathcal{A} = 1 \text{ Bq/m}^3$.

The detector response is assumed to be proportional with a resolution driven by the photoelectron statistics (see e.g. Knoll [52]). Thus, the reconstructed energy, denoted by ν_r , follows a normal distribution, as

$$\mathcal{N}(\nu_r; \Delta) = \frac{1}{\sqrt{2\pi}\sigma} e^{-\frac{(\nu_r - \Delta)^2}{2\sigma^2}}, \quad (37)$$

where Δ is the actual energy deposited in the NaI(Tl) scintillator, as determined by the Monte Carlo simulation. The resolution factor σ can be expressed as

$$\sigma(\Delta) = 2\sqrt{2 \ln 2} \epsilon_0 \sqrt{\Delta \Delta_0}, \quad (38)$$

where $\Delta_0 = 0.6617 \text{ MeV}$ is the ^{137}Cs major emission line. The energy resolution is set to $\epsilon_0 = 6.7\%$, according to a least square fit of the experimental values reported by Duc Tam et al. [51].

A Monte Carlo estimate of the differential counting rate is given by

$$\frac{dR}{d\nu_r} \simeq \frac{1}{N} \sum_{i=1}^N \omega_i(\Delta_i) \mathcal{N}(\nu_r; \Delta_i), \quad (39)$$

where the summation runs over the N generated Monte Carlo events with Monte Carlo weights ω_i . It should be noted that the previous eq. 39 directly provides the differential counting rate, w.r.t. ν_r , in the form of a Kernel Density Estimate (KDE). Thus, we do not randomise the reconstructed energy event by event, which would unnecessarily increase the Monte Carlo variance and also require a histogram. Instead, we repeat applying eq. 39 by varying ν_r over a grid of values (linearly spaced).

The end-to-end forward simulation is carried out using CALZONE v1.1.1 [38] (i.e. GEANT4 11.2.1), with Penelope Physics. In this case, the Monte Carlo weight simply writes as

$$\omega_i(\Delta_i) = \begin{cases} V_0 \mathcal{A} I & \text{if } \Delta_i > 0, \\ 0 & \text{otherwise,} \end{cases} \quad (40)$$

where V_0 is the source volume, \mathcal{A} its volume activity and $I = 1.597$ its total gamma-ray intensity (see Table 1). In the mixed case, intermediary photons are generated over an envelope tightly bounding the detector. This envelope encompasses the scintillator volume as well as an aluminium oxide reflector (2-3 mm thick) and an aluminium housing (1.5 mm thick). As outlined in section 3.4.2, the intermediary photons are then transported backwards using GOUPIL, which provides the Monte Carlo weights ω_i , and forward simulated through the detector using CALZONE, which provides the energies Δ_i deposited in the NaI(Tl) scintillator.

5.2.2. Comparison of performances

The statistics and performances of the Test 2 Monte Carlo simulations are summarised in Table 4, employing the same metrics as for Test 1. Notably, the mixed simulation is approximately 10^3 times faster than the end-to-end forward simulation. While the gain is less pronounced than in an in-air detector scenario (i.e. Test 1), it remains appreciable. This outcome was anticipated, given that the source and detector are more comparable in size to those in Test 1. It is also noteworthy that the GOUPIL backward transport stage accounts for only a few percent of the total CPU time in the mixed case. Consequently, the relative CPU gain in mixed mode is seldom influenced by the GEANT4 physics list.

In mixed mode, 64% of the intermediary photons are absorbed before ever reaching the scintillator, during the forward simulation. Of the remaining 36% of photons, 82% successfully sample a source during the backward stage, resulting in an overall Monte Carlo efficiency of 30%.

Table 4: Statistics of Test 2 Monte Carlo simulations conducted on the HPC2 computing grid of the Clermont-Auvergne mesocentre. The table indicates the number of generated events N , the Monte Carlo efficiency ϵ (i.e. the ratio of the number of gamma-rays depositing energy in the NaI(Tl) scintillator to the number generated), the average simulation time Δt_0 per generated event, and the average time $\Delta t_1 = \Delta t_0/\epsilon$ per detected gamma-ray. Version 1.1.1 of CALZONE was used (i.e. GEANT4 11.2.1) with Penelope Physics.

Simulation	N	ϵ	Δt_0	Δt_1
Forward	$9.5 \cdot 10^{10}$	$8.9 \cdot 10^{-4}$	0.18 ms	0.20 s
Mixed	$2.2 \cdot 10^8$	$3.0 \cdot 10^{-1}$	59 μ s	0.20 ms

Substituting a 1 km radius sphere of air for the 1 m radius water source has no effect on the overall Monte Carlo efficiency in mixed mode. On the contrary, in the case of an end-to-end forward simulation, only 14 energy deposits were collected out of $1.2 \cdot 10^{10}$ generated gamma-rays. This indicates that the CPU-gain would exceed $\sim 10^8$ for a scintillator completely immersed in air. Yet, the important point in practice, is that such simulations are simply unattainable with conventional methods and computing resources, whereas with the mixed procedure one can already achieve decent results (thousands of detected events per second) using only a laptop.

5.2.3. Comparison of results

The differential counting rates $dR/d\nu_r$ obtained with both procedures are reported on figure 9. The mixed procedure reproduces the end-to-end forward results to within 1 %, with the exception of the 511 keV region, corresponding to gamma-rays emitted by positrons annihilating in the water volume surrounding the detector (which cannot be simulated by GOUPIIL, since secondaries are neglected).

Finally, it is worth noting that the generation of intermediate photons directly on the scintillator volume (instead of on the detector envelope) leads to an additional bias of ~ 1 %. While the two volumes only differ by a few millimetres of aluminium, which is sufficient to stop a 1 MeV electron, the secondaries produced in this thin layer (containing the reflector and housing) do slightly contribute to the detector response.

6. Conclusion

In this article, we presented a simple modification (alg. 2) to our backward Monte Carlo transport algorithm (Niess et al. [29]) allowing for discrete energy sources. This modification has been implemented in the GOUPIIL software library for the Monte Carlo transport of low-energy gamma photons, typically from radioactive isotopes. The modified algorithm performs well with comparable computing times per event (Δt_0) to the forward mode (see e.g. table 2), and an accuracy within one per cent.

GOUPIIL has a clear advantage over conventional transport engines due to its high Monte Carlo efficiency in backward mode. With forward simulations, when the source volume exceeds the detector size, the efficiency may decrease significantly. This is particularly evident for gamma-rays transported through the atmosphere, with Monte Carlo efficiencies, ϵ , that can drop as low as $\mathcal{O}(10^{-9})$. On the contrary, in backward mode GOUPIIL maintains efficiencies of $\mathcal{O}(1)$.

It is important to note that GOUPIL is not intended to provide a complete framework, such as a Monte Carlo simulation of the response of a gamma-ray spectrometer. Instead, generalist software packages (e.g. FLUKA, GEANT4, MCNP or PENELOPE) might be utilised for this purpose. GOUPIL is a specialized software package that significantly accelerates the transport of gamma photons in certain circumstances, as previously discussed. It is expected that GOUPIL is used in conjunction with a detector model or another simulation tool. For the latter case, GOUPIL provides a C interface that allows for the injection of an external geometry engine. The `goupil` Python module includes an adapter to GEANT4 that utilises this C interface.

In particular, GOUPIL is interoperable with CALZONE [38], a GEANT4 Python wrapper that was developed in conjunction with this work in order to facilitate the building of mixed simulations. An example of such a mixed simulation, employing a scintillation detector, was presented in section 5.2. It was demonstrated that, apart from the 511 keV photopeak resulting from positron annihilation, the mixed simulation procedure reproduces the outcomes of an end-to-end forward simulation while achieving events rates of a few kHz (see Δt_1 in Table 4) with a ~ 2.3 GHz CPU. However, it should be recalled that, in order to achieve such performances, the source region must substantially encompass the detector.

This paper presented a comprehensive academic description of GOUPIL, covering its algorithms and implementation. For practical guidance on using GOUPIL, please consult the available online documentation [37].

CRediT authorship contribution statement

Valentin Niess: Conceptualization, Methodology, Software, Validation, Formal analysis, Writing – Original Draft, Writing – Review & Editing, Visualization. **Kinson Vernet:** Software, Validation, Formal analysis, Writing – Review & Editing, Visualization. **Luca Terray:** Conceptualization, Resources, Writing – Review & Editing, Project administration, Funding acquisition.

Declaration of Generative AI and AI-assisted technologies in the writing process

During the preparation of this work the authors used DEEPL in order to translate the manuscript from French to English. After using this tool, the authors reviewed and edited the content as needed and take full responsibility for the content of the publication.

Acknowledgements

We gratefully acknowledge support from the Mésocentre Clermont-Auvergne of the University of Clermont Auvergne for providing computing resources needed for this work. This is contribution no. 673 of the ClerVolc program of the International Research Center for Disaster Sciences and Sustainable Development of the University of Clermont Auvergne. The analysis of Monte Carlo data has been done with numpy [53]. Validation figures have been produced with matplotlib [54].

Appendix A. Constrained backward collision

In order to prove that algorithm 2 is correct, it is instructive to consider the more general procedure described below (alg. 4). With the latter method, a constrained backward collision procedure is constructed from an unconstrained one, noted RANDOMISEBACKWARD, using a Russian Roulette method. For simplicity, in algorithm 4 we have omitted the index j of the interaction process and the angular coordinate \mathbf{u} , as they are not relevant (see [29, Appendix D] for example).

Algorithm 4 produces two collision topologies, which depends on the branch of line L2 or L6. The first topology corresponds to the collision of a photon emerging from a point source of energy ν_I . This branch also determines the end of the backward trajectory simulation, which justifies the name *Russian Roulette*. The second topology simulates the backward collision of a photon from an energy-distributed source on $[\nu_i, \nu_I]$. This branch generates an internal collision vertex of the trajectory. Algorithm 4 is correct provided that it assigns the appropriate weighted probability densities to each branch, following equation 13. For the first branch, this condition is trivially satisfied. For the second branch, it is important to note that the rejection method used at line L7 selects a pre-collision energy ν_{i-1} based on the PDF

$$p_r^*(\nu_{i-1}; \nu_i, \nu_I) = \frac{p_c^*(\nu_{i-1}; \nu_i)}{P_c^*(\nu_I; \nu_i)}, \quad (\text{A.1})$$

This justifies the weighting applied at line L11.

Algorithm 4 is thus compliant, in the sense that it backwards generates the correct collision topologies and with the correct weights. However, it requires an adjustment parameter q , which affects its effectiveness. Note that this parameter q can be a function of the post-collision energy, ν_i , which is actually an input parameter to the backward procedure. It seems appropriate for $q \rightarrow 1$ to let $\nu_i \rightarrow \nu_I$. Furthermore, the energy before collision, ν_{i-1} , might be bounded by the kinematics of the collision, for a given value of ν_i . Let us denote this bound $\nu_{\max}(\nu_i)$. Now, for $\nu_{\max} < \nu_I$, it is desirable that $q = 0$, because otherwise the first branch of algorithm 4 could return physically impossible events. Although these events have zero weight, it is not efficient to generate them.

A suitable option, which meets the aforementioned criteria, is to equal q and the rejection probability, as

$$q(\nu_i, \nu_I) = 1 - P_c^*(\nu_I; \nu_i). \quad (\text{A.2})$$

This choice eliminates the weighting of line L11 but most importantly it also let us eliminate the inner loop (L7). This results in algorithm 2.

Appendix B. Continuous absorption

A valid backward-absorption method shall restore the appropriate weighted probability density for T -trajectories, as per $p^*\omega = p$. That for, it is worth noticing that the absorption cross-section does not appear in the collision term c which is used to express p (see eq. 7). Thus, absorption could be treated as a continuous process rather than a discrete collision. To clarify, let Λ_c be the mean free path obtained by excluding absorption processes, and let $\mathbf{\Lambda}_c$ be the corresponding vector of Λ_j values, where j indexes processes.

Assuming no absorption, a backward simulation procedure verifies $p^*[\Lambda_c]\omega[\Lambda_c] = p[\Lambda_c]$ for any T -trajectory. By definition,

$$P_s[\Lambda] = P_s[\Lambda_a]P_s[\Lambda_c], \quad (\text{B.1})$$

where Λ is the total mean free path. Since the collision term c is independent of the absorption processes,

$$p[\Lambda] = P_s[\Lambda_a]p[\Lambda_c]. \quad (\text{B.2})$$

Therefore, by applying an additional weighting

$$\omega \leftarrow P_s[\Lambda_a]\omega, \quad (\text{B.3})$$

one reproduces the PDF $p[\Lambda]$.

In practice, the absorption weight, $\omega_a = P_s[\Lambda_a]$, can be built up step-by-step during the simulation, by weighting the flight between two successive vertices by the probability of survival of the photon according to the absorption processes alone. Note that this continuous treatment of absorption processes can be applied during both backward and forward simulations (resulting in a non-analogue forward simulation).

Appendix C. Backward photo-peaks

Backward generated photo-peak trajectories differ from forward ones only by an additional incomplete collision vertex. Thus, the collision factor of a backward trajectory writes

$$c^*(\mathbf{S}) = c_0^*(S_I)c(\mathbf{S}), \quad (\text{C.1})$$

where $c_0^*(S_I) = 1/\lambda_{\text{in}}(\mathbf{r}_I, \nu_I)$, since inelastic collisions are considered as a single process in this case, and since these collisions are not simulated. Thus,

$$p^*(\mathbf{S}) = \frac{p(\mathbf{S})}{\lambda_{\text{in}}(\mathbf{r}_I, \nu_I)}, \quad (\text{C.2})$$

which completes the proof.

Appendix D. Merging of atomic cross-sections

Let x_i^k denote the sequence of energies, ordered by increasing values, at which the atomic-cross section σ^k was computed (the process index j being omitted). Thus, at a discontinuity one has $x_i^k = x_{i+1}^k$, but $\sigma_i^k \neq \sigma_{i+1}^k$. The combined mesh y_ℓ , representing the sequence of energies for the material cross-section σ , is constructed as the increasing ordered sequence of all the x_i^k values, merged over k . Furthermore, let us require that a point y_ℓ is duplicated if and only if it corresponds to a discontinuity in at least one of the σ^k . Once the combined mesh has been constructed, the values σ_ℓ of the material cross-section at mesh points are computed according to equation 21. This sometimes implies interpolating σ^k at y_ℓ . In addition, at the left-hand side (right-hand side) of a discontinuity in σ , one must take care to use the corresponding left (right) value of σ^k .

Appendix E. Sampling of Rayleigh collisions

To sample q^2 and $\cos \theta$ in a Rayleigh collision, a rejection method is employed. Let us observe that the function $f = |F/Z|$ is bounded by the function g defined as

$$g(q, Z) = \frac{q_0^2(Z)}{q_0^2(Z) + q^2}, \quad \text{where} \quad q_0^2(Z) = \sup_{q>0} \frac{q^2 f(q, Z)}{1 - f(q, Z)}. \quad (\text{E.1})$$

The bound $|g|^2$ is an analytical function that allows for easy sampling of q^2 values, such as through the CDF-inverse method. This results in the algorithm 5 below.

This algorithm differs from the implementation of PENELOPE, which samples q^2 directly according to $|F|^2$. The latter however requires the whole CDF of $|F|^2$ to be tabulated instead of a single parameter, q_0^2 . On the other hand, GOUPIL method is slower because the probability of selecting r (L9) is lower by a factor of $f/g \leq 1$. We have found that this effect is anecdotal for our applications, as Rayleigh collisions are infrequent compared with other processes. Thus, GOUPIL uses algorithm 5 because of its small memory footprint while being sufficiently fast.

Appendix F. Sampling of forward Compton collisions

By default, GOUPIL uses a rejection method in order to sample the energy of the emerging photon, in a Compton collision. Let us point out that the scattering function $S_\nu \in [0, 1]$ decreases with ν_i . Consequently, ν_i is sampled according to the matrix element M , using the method described in Butcher and Messel [55], but with an additional selection factor accounting for S_ν as

$$q(\nu_{i-1}, \nu_i) = \frac{S_\nu(\nu_{i-1}, \nu_i)}{S_\nu(\nu_{i-1}, \nu_{\min}(\nu_{i-1}))}. \quad (\text{F.1})$$

The factor q decreases with ν_{i-1} , making the rejection method inefficient at low energies. In practice, this is counterbalanced by the fact that absorption then becomes predominant.

An alternative method for sampling ν_i , which is also implemented in GOUPIL, is to use the inverse transform technique. Numerically, the quantiles of the distribution function of ν_i are tabulated for different values of ν_{i-1} , and then this table is interpolated during the simulation of a collision. We have found that this method saves a factor of ~ 2 in simulation time for transporting a $1/\nu_I$ flux in a uniform medium. However, in more realistic scenarios, the gain will inevitably be lower due to the resolution of the geometry impacting performances. Additionally, to achieve satisfactory numerical accuracy using the inverse transform method, exhaustive tables containing $\mathcal{O}(10^5)$ values per material must be generated. Thus, GOUPIL uses the rejection method by default, which is expected to be sufficiently fast for most use cases.

Appendix G. Sampling of adjoint Compton collisions

In the case of the adjoint process (eq. 30), the energy ν_{i-1} of the incident photon is sampled using a rejection method. The method is similar to the forward case, but the

PDF of the generating process is proportional to M/ν_{i-1}^3 instead of M . Additionally, the selection probability q accounting for the scattering function S_ν is modified as

$$q(\nu_{i-1}, \nu_i) = \frac{S_\nu(\nu_{i-1}, \nu_i)}{S_\nu(\nu_{\max}^*(\nu_i), \nu_i)}, \quad (\text{G.1})$$

since S_ν increases according to ν_{i-1} . The weight, ω_c , is calculated on the fly from the tabulated forward ($\sigma(\nu_{i-1})$) and adjoint ($\sigma^*(\nu_i)$) cross-section values.

Let us point out that the inverse transform method can also be used to simulate the adjoint process with GOUPIL, by tabulating the quantiles of the adjoint PDF, $p_c^* = (1/\sigma^*)d\sigma^*/d\nu_{i-1}$. However, the rejection method is used by default in order to minimise memory usage, as in the forward case.

Appendix H. Sampling of backward Compton collisions

Let $P_c(\nu_i; \nu_{i-1})$ represent the CDF of ν_i in a forward Compton collision. Assuming that $d\sigma/d\nu_i > 0$, it follows that $P_c(\nu_i; \nu_{i-1})$ strictly increases with ν_i on the support (ν_{\min}, ν_{\max}) . It can also be observed that P_c is strictly decreasing with ν_{i-1} on the support $(\nu_{\min}^*, \nu_{\max}^*)$. Thus, the relation

$$P_c(\nu_i; \nu_{i-1}) = \zeta, \quad \zeta \in [0, 1], \quad (\text{H.1})$$

establishes a bijection between ν_{i-1} and ν_i for a given ζ value. As a result, the inverse transform method is applicable to both the forward process (by inverting equation H.1 according to ν_i) and the backward process (by inverting according to ν_{i-1}). Furthermore, if we denote $\nu^{-1}(\nu_i; \zeta)$ the inverse bijection, the Monte Carlo weight for a backward collision is given by Niess et al. [29, lemme 1] (equation 15).

Technically, the sampling of the backward process is almost identical to the forward case (Appendix F). However, one needs to tabulate not only the quantiles with respect to ν_{i-1} , but also the ω_c weights. These weights are determined by the slope of the cubic interpolations of ν^{-1} for different ζ values of the CDF. Like the forward case, these tabulations require a large number of values to achieve decent numerical accuracy. Therefore, this technique is not the default method used by GOUPIL.

References

- [1] R. L. Grasty, *Geophysics* 40 (1975) 503–519.
- [2] Y. Sanada, T. Torii, J. Environ. Radioact. 139 (2015) 294–299. <https://doi.org/10.1016/j.jenvrad.2014.06.027>.
- [3] R. L. Grasty, J. Hovgaard, J. Multala, *Radiat. Prot. Dosim.* 73 (1997) 225–230. <https://doi.org/10.1093/oxfordjournals.rpd.a032139>.
- [4] P. P. Povinec, I. Osvath, M. S. Baxter, *Appl. Radiat. Isot.* 47 (1996) 1127–1133. [https://doi.org/10.1016/S0969-8043\(96\)00118-2](https://doi.org/10.1016/S0969-8043(96)00118-2).
- [5] H. Zafrir, G. Haquin, U. Malik, et al., *Radiat. Meas.* 46 (2011) 611–620. <https://doi.org/10.1016/j.radmeas.2011.04.027>.
- [6] M. Baldoncini, M. Albéri, C. Bottardi, et al., *Atmospheric Environ.* 170 (2017) 259–268. <https://doi.org/10.1016/j.atmosenv.2017.09.048>.
- [7] H. Dulai, J. Kamenik, C. A. Waters, et al., *J. Radioanal. Nucl. Chem.* 307 (2016) 1865–1870. <https://doi.org/10.1007/s10967-015-4580-9>.
- [8] N. Takeuchi, A. Katase, *J. Nucl. Sci. Technol.* 19 (1982) 393–409. <https://doi.org/10.1080/18811248.1982.9734160>.

- [9] N. Reinhardt, L. Herrmann, J. Plant Nutr. Soil Sci. 182 (2019) 9–27. <https://doi.org/10.1002/jpln.201700447>.
- [10] L. Terray, P.-J. Gauthier, V. Breton, et al., J. Geophys. Res. Solid 125 (2020) e2019JB019149. <https://doi.org/10.1029/2019JB019149>.
- [11] B. R. S. Minty, AGSO J. Aust. Geol. Geophys. 17 (1997) 39–50.
- [12] S. Agostinelli, J. Allison, K. Amako, et al., Nucl. Instrum. Methods. Phys. Res. A 506 (2003) 250–303. [https://doi.org/10.1016/S0168-9002\(03\)01368-8](https://doi.org/10.1016/S0168-9002(03)01368-8).
- [13] J. Allison, K. Amako, J. Apostolakis, et al., IEEE Trans. Nucl. Sci. 53 (2006) 270–278. <https://doi.org/10.1109/TNS.2006.869826>.
- [14] J. Allison, K. Amako, J. Apostolakis, et al., Nucl. Instrum. Methods. Phys. Res. A 835 (2016) 186–225. <https://doi.org/10.1016/j.nima.2016.06.125>.
- [15] M. E. Rising, J. C. Armstrong, S. R. Bolding, et al., Technical Report LA-UR-22-33103, Rev. 1, Los Alamos National Laboratory, 2023. <https://doi.org/10.2172/1909545>.
- [16] C. Bagatelas, C. Tsabaris, M. Kokkoris, et al., Environ. Monit. Assess. 165 (2010) 159–168. <https://doi.org/10.1007/s10661-009-0935-4>.
- [17] E. G. Androulakaki, M. Kokkoris, C. Tsabaris, et al., Appl. Radiat. Isot. 114 (2016) 76–86. <https://doi.org/10.1016/j.apradiso.2016.05.008>.
- [18] M. Baldoncini, M. Albéri, C. Bottardi, et al., J. Environ. Radioact. 192 (2018) 105–116. <https://doi.org/10.1016/j.jenvrad.2018.06.001>.
- [19] D. Satoh, K. Kojima, A. Oizumi, et al., J. Nucl. Sci. Technol. 51 (2014) 656–670. <https://doi.org/10.1080/00223131.2014.886534>.
- [20] L. E. Smith, C. J. Gesh, R. T. Pagh, et al., IEEE Trans. Nucl. Sci. 55 (2008) 2598–2606. <https://doi.org/10.1109/TNS.2008.2002819>.
- [21] M. W. Shaver, L. E. Smith, R. T. Pagh, et al., Nucl. Technol. 168 (2009) 95–100. <https://doi.org/10.13182/NT09-A9106>.
- [22] D. Gabler, J. Henniger, U. Reichelt, Nucl. Instrum. Method Phys. Res. Sect. B Beam Interact. Mater. At. 251 (2006) 326–332. <https://doi.org/10.1016/j.nimb.2006.07.005>.
- [23] P. Pourrouquet, J.-C. Thomas, P.-F. Peyrard, et al., in: 2011 IEEE Radiation Effects Data Workshop, 2011, pp. 1–5. <https://doi.org/10.1109/REDW.2010.6062530>.
- [24] A. P. Robinson, D. Henderson, L. Kersting, E. Moll, Nucl. Sci. Eng. 196 (2022) 1–15. <https://doi.org/10.1080/00295639.2021.1935103>.
- [25] A. Malins, M. Machida, K. Niita, EPJ Web Conf. 153 (2017) 06001. <https://doi.org/10.1051/epjconf/201715306001>.
- [26] L. Desorgher, F. Lei, G. Santin, Nucl. Instrum. Methods. Phys. Res. A 621 (2010) 247–257. <https://doi.org/10.1016/j.nima.2010.06.001>.
- [27] M. D. Looper, Technical Report ATR-2018-00052, Aerospace Corp El Segundo, CA, El Segundo, United States, 2018.
- [28] B. Jun, B. X. Zhu, L. M. Martinez-Sierra, I. Jun, IEEE Trans. Nucl. Sci. 67 (2020) 1629–1636. <https://doi.org/10.1109/TNS.2020.2979657>.
- [29] V. Niess, A. Barnoud, C. Cârloganu, E. Le Ménédeu, Comput. Phys. Commun. 229 (2018) 54–67. <https://doi.org/10.1016/j.cpc.2018.04.001>.
- [30] V. Niess, Comput. Phys. Commun. 279 (2022) 108438. <https://doi.org/10.1016/j.cpc.2022.108438>.
- [31] Lara, 2023. <http://www.lnhb.fr/accueil/donnees-nucleaires/module-lara/>.
- [32] D. E. Cullen, J. H. Hubbell, L. Kissel, EPDL97, Technical Report, LLNL, 1997.
- [33] M. J. Berger, Methods in Computational Physics 1 (1963) 135–215.
- [34] Rust Programming Language, 2023. <https://www.rust-lang.org/>.
- [35] Python Package Index, Goupil, 2024. <https://pypi.org/project/goupil/>.
- [36] Github, Goupil, 2024. <https://github.com/niess/goupil/>.
- [37] Read the Docs, Goupil, 2024. <https://goupil.readthedocs.io/en/latest/>.
- [38] Github, Calzone, 2025. <https://github.com/niess/calzone/>.
- [39] J. Baró, J. Sempau, J. M. Fernández-Varea, F. Salvat, Nucl. Instrum. Methods. Phys. Res. B 100 (1995) 31–46. [https://doi.org/10.1016/0168-583X\(95\)00349-5](https://doi.org/10.1016/0168-583X(95)00349-5).
- [40] F. Salvat, Penelope-2014: A code system for monte carlo simulation of electron and photon transport, 2015. <https://www.oecd-neo.org/lists/penelope.html>.
- [41] R. L. Workman, V. Burkert, V. Crede, et al. (Particle Data Group), PTEP 2022 (2022) 083C01. <https://doi.org/10.1093/ptep/ptac097>.
- [42] D. Higham, J. Comput. Appl. Math. 39 (1992) 287–294. [https://doi.org/10.1016/0377-0427\(92\)90205-C](https://doi.org/10.1016/0377-0427(92)90205-C).

- [43] EPICS, 2023. <https://www-nds.iaea.org/epics/>.
- [44] M. Berger, J. Hubbell, S. Seltzer, et al., 2010. <https://doi.org/10.18434/T48G6X>.
- [45] M. Born, Atomic Physics, Blackie and Son, 1969.
- [46] O. Klein, Y. Nishina, Z. für Phys. 52 (1929) 853–868. <https://doi.org/10.1007/BF01366453>.
- [47] J. Baró, M. Roteta, J. M. Fernández-Varea, F. Salvat, Radiat. Phys. Chem. 44 (1994) 531–552. [https://doi.org/10.1016/0969-806X\(94\)90053-1](https://doi.org/10.1016/0969-806X(94)90053-1).
- [48] R. Ribberfors, K. F. Berggren, Phys. Rev. A 26 (1982) 3325–3333. <https://doi.org/10.1103/PhysRevA.26.3325>.
- [49] V. Niess, A. Barnoud, C. Cârloganu, O. Martineau-Huynh, Comput. Phys. Commun. 247 (2020) 106952. <https://doi.org/10.1016/j.cpc.2019.106952>.
- [50] Mésocentre Clermont-Auvergne, 2024. <https://mesocentre.uca.fr/>.
- [51] H. Duc Tam, N. T. Hai Yen, L. B. Tran, H. Dinh Chuong, T. Thien Thanh, Appl. Radiat. Isot. 130 (2017) 75–79. <https://doi.org/10.1016/j.apradiso.2017.09.020>.
- [52] G. F. Knoll, Radiation detection and measurement, John Wiley & Sons, 2010.
- [53] C. R. Harris, K. J. Millman, S. J. van der Walt, et al., Nature 585 (2020) 357–362. <https://doi.org/10.1038/s41586-020-2649-2>.
- [54] J. D. Hunter, Comput. Sci. Eng. 9 (2007) 90–95. <https://doi.org/10.1109/MCSE.2007.55>.
- [55] J. Butcher, H. Messel, Nucl. Phys. 20 (1960) 15–128. [https://doi.org/10.1016/0029-5582\(60\)90162-0](https://doi.org/10.1016/0029-5582(60)90162-0).

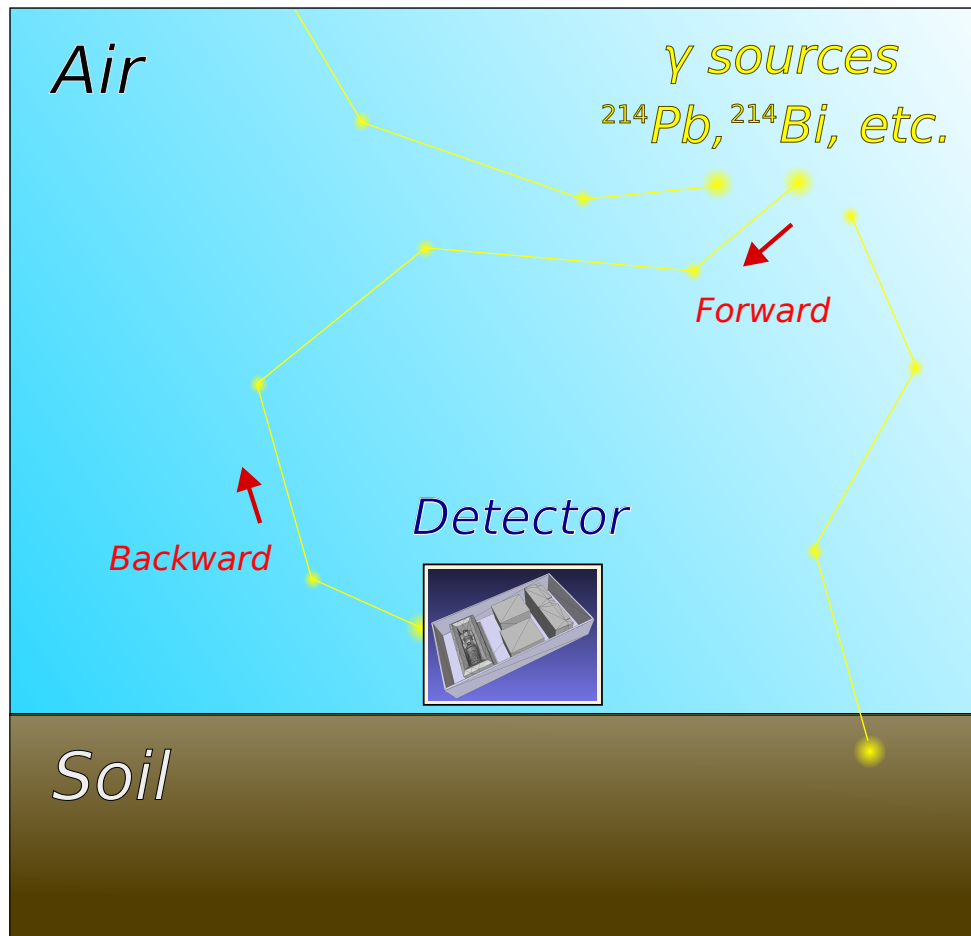


Figure 1: Schematic view of the Monte Carlo transport of gamma photons emitted by radionuclides. Yellow lines represent Monte Carlo trajectories, and yellow dots indicate collision vertices. Gamma photons follow rectilinear trajectories between two vertices.

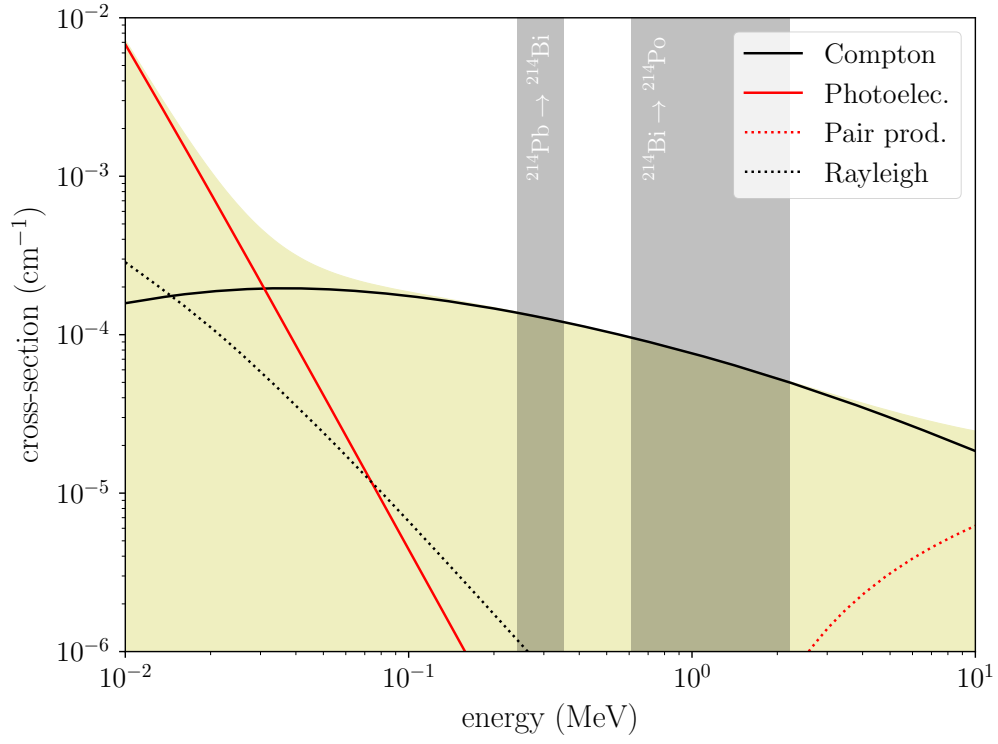


Figure 2: Macroscopic cross-sections for photon interactions in dry air at 1 bar ($\rho = 1.205 \text{ mg/cm}^3$), as per the EPDL (Cullen et al. [32]). The total cross-section is represented by the yellow shaded area, which is obtained by summing the four processes shown in the figure. The grey vertical bands indicate the energy ranges of the gamma emissions associated with the $^{214}\text{Pb} \rightarrow ^{214}\text{Bi}$ and $^{214}\text{Bi} \rightarrow ^{214}\text{Po}$ decays, according to table 1.

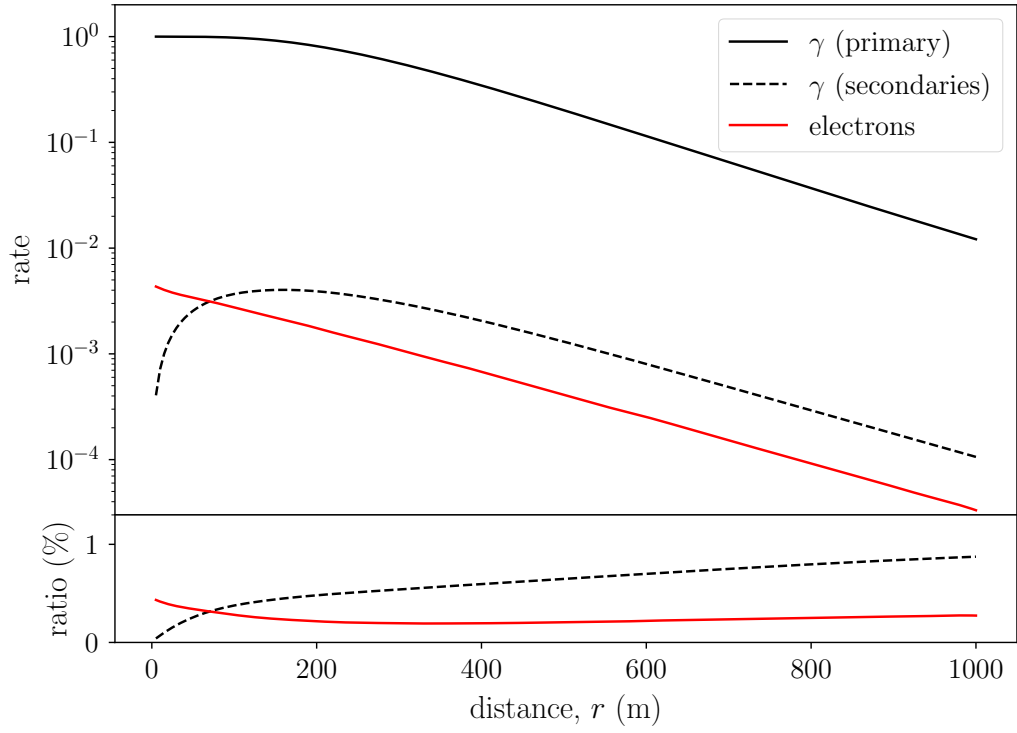


Figure 3: Normalised rate of outgoing particles at a distance r from the source for the synthetic experiment described in the text (GEANT4 10.7.4, `G4EmStandardPhysics`). The lower frame displays the ratio to primary photons as a percentage. The positron flux is negligible compared to that of the electrons and secondary photons.

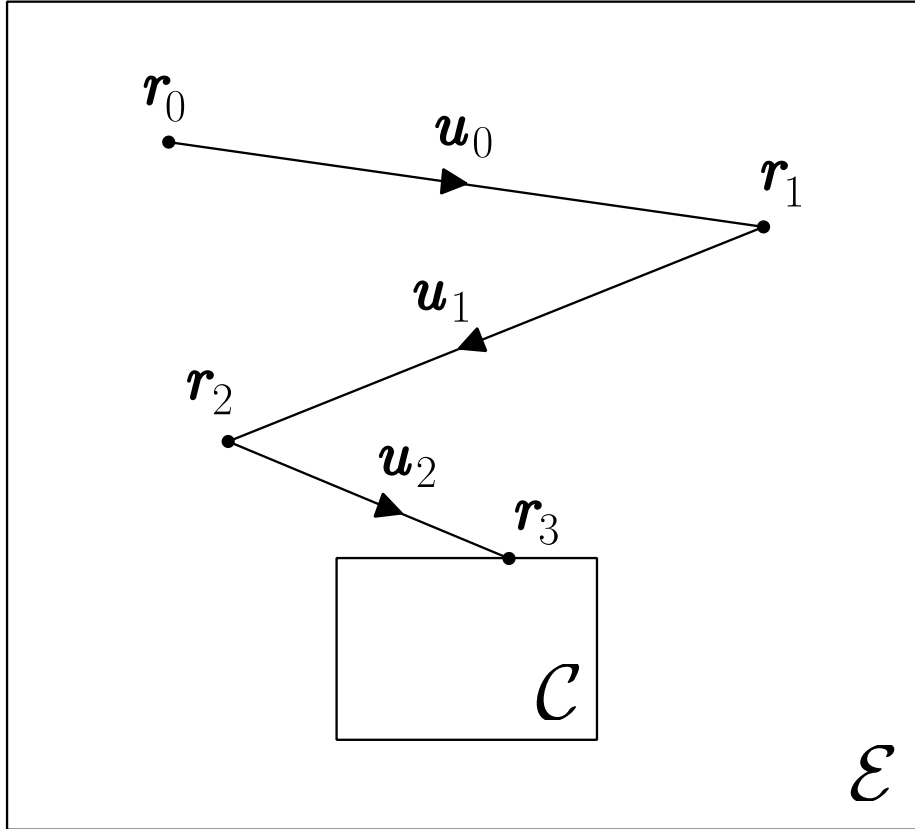


Figure 4: Example of a 2D Monte Carlo trajectory that was produced at point \mathbf{r}_0 . The trajectory reaches the collection surface \mathcal{C} at point \mathbf{r}_3 after two collisions, at \mathbf{r}_1 and \mathbf{r}_2 . The collection surface (\mathcal{C}) and the external surface (\mathcal{E}) are represented by rectangles.

Algorithm 3 Backward Monte Carlo transport.

Require: $\nu_I \geq \nu_{n+1} > 0$, $\|\mathbf{u}\| = 1$, $\sigma_j > 0 \forall j$, \mathcal{R} (a random stream).

```

1:  $(\nu, \mathbf{r}, \mathbf{u}) \leftarrow (\nu_{n+1}, \mathbf{r}_{n+1}, \mathbf{u}_{n+1})$  ▷ Initialisation to arrival parameters.
2:  $\omega \leftarrow 1$ 
3:  $\boldsymbol{\sigma} \leftarrow \text{CROSSSECTIONS}(\nu)$ 
4:  $\sigma \leftarrow \text{SUM}(\boldsymbol{\sigma})$ 
5: loop
6:    $\Lambda \leftarrow \frac{M}{N_A \sigma}$ 
7:    $\zeta \leftarrow \text{OPEN01}(\mathcal{R})$ 
8:    $X \leftarrow -\Lambda \ln \zeta$ 
9:    $d_V \leftarrow \text{DISTANCETOVERTEX}(\mathbf{r}, -\mathbf{u}, X)$ 
10:   $d_I \leftarrow \text{DISTANCETOINTERFACE}(\mathbf{r}, -\mathbf{u})$ 
11:  if  $d_I < d_V$  then ▷ Stop on an interface.
12:     $\mathbf{r} \leftarrow \mathbf{r} - d_I \mathbf{u}$ 
13:    return  $(\nu, \mathbf{r}, \mathbf{u}, \omega)$ 
14:  else
15:     $\mathbf{r} \leftarrow \mathbf{r} - d_V \mathbf{u}$ 
16:  end if
17:   $j \leftarrow \text{SELECTPROCESS}(\boldsymbol{\sigma}, \sigma, \mathcal{R})$ 
18:  if  $j \in \text{ABSORPTION}$  then ▷ Stop by absorption.
19:    return  $(0, \mathbf{r}, \mathbf{u}, 0)$ 
20:  else if  $j \in \text{ELASTIC}$  then
21:     $(\cdot, \mathbf{u}) \leftarrow \text{RANDOMISECOLLISION}(j, \nu, \mathbf{u}, \mathcal{R})$ 
22:  else if  $\nu = \nu_I$  then ▷ Stop on a source.
23:     $\rho \leftarrow \text{DENSITY}(\mathbf{r})$ 
24:     $\sigma_{\text{in}} \leftarrow \text{SUM}(\boldsymbol{\sigma}(\text{INELASTIC}))$ 
25:     $\lambda_{\text{in}} \leftarrow \frac{M}{\rho N_A \sigma_{\text{in}}}$ 
26:     $\omega \leftarrow \lambda_{\text{in}} \omega$ 
27:    return  $(\nu, \mathbf{r}, \mathbf{u}, \omega)$ 
28:  else
29:     $(\nu, \mathbf{u}, \omega_c) \leftarrow \text{RANDOMISECONSTRAINED}(j, \nu, \nu_I, \mathcal{R})$ 
30:     $\sigma_j \leftarrow \boldsymbol{\sigma}(j)$ 
31:     $\boldsymbol{\sigma} \leftarrow \text{CROSSSECTIONS}(\nu)$ 
32:     $\sigma \leftarrow \text{SUM}(\boldsymbol{\sigma})$ 
33:     $\omega \leftarrow \omega_c \frac{\sigma(j)}{\sigma_j} \omega$ 
34:  end if
35: end loop

```

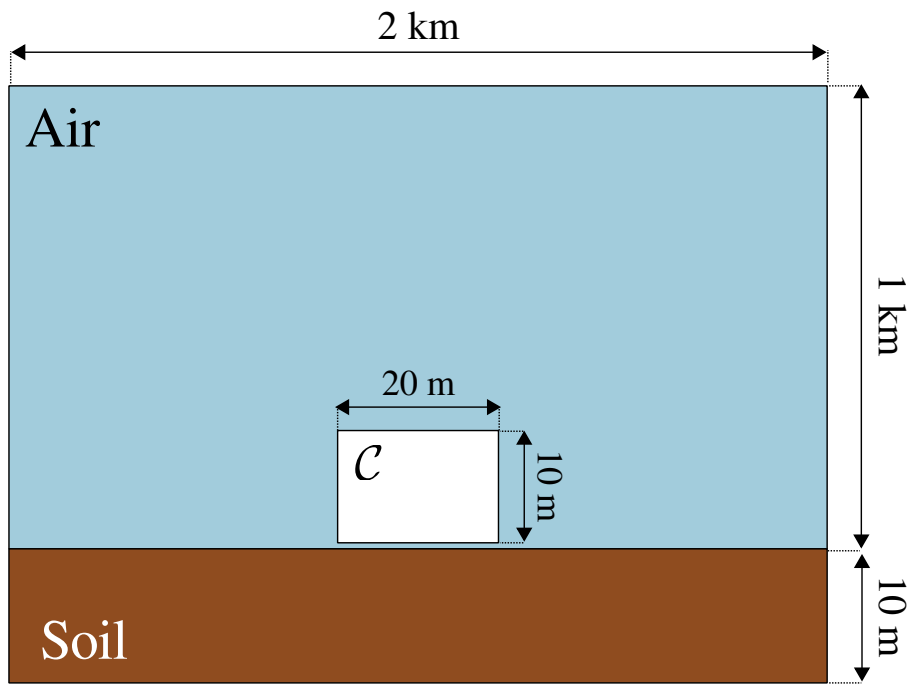


Figure 5: Schematic cross-section of the test geometry in the (xOz) plane. The white internal parallelepiped represents the collection volume delimited by the surface \mathcal{C} . The dimensions of the air, soil, and collection volumes are not to scale.

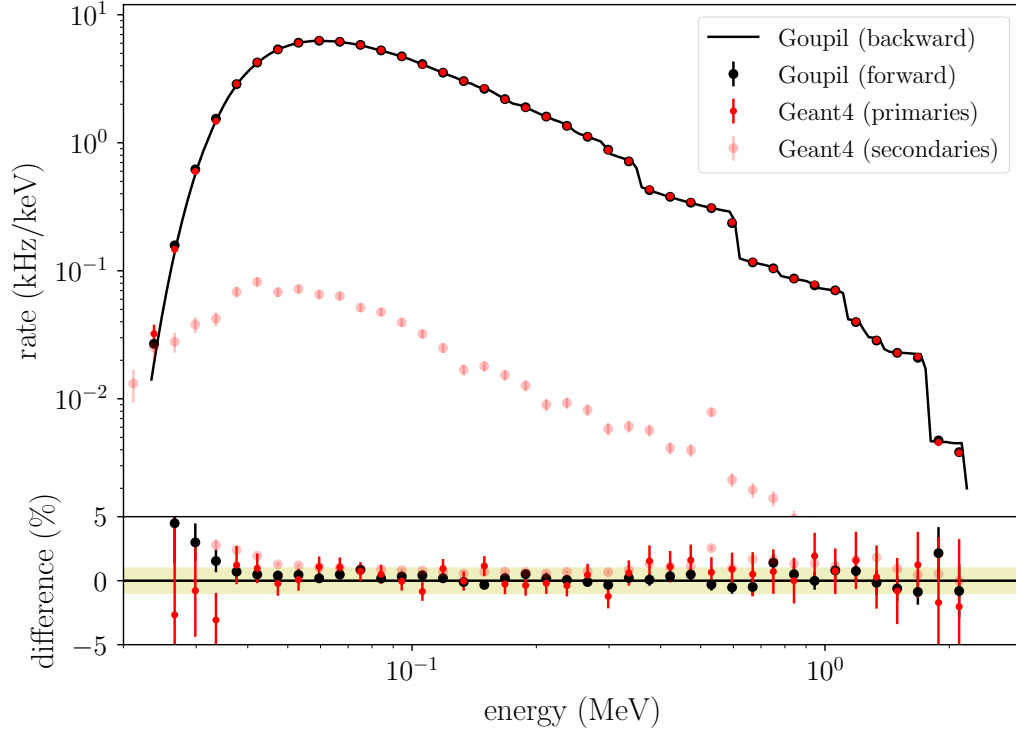


Figure 6: Background energy spectrum (B) of gamma-rays collected on the inner surface (C) of the Test 1 geometry. The secondary flux (γ , e^- , e^+) obtained with GEANT4 is also shown for comparison. The error bars indicate Monte Carlo uncertainties at 68% confidence. The bottom inset displays the relative deviation w.r.t. the results obtained with GOUPI used in backward mode. The yellow band indicates a relative deviation of less than 1%.

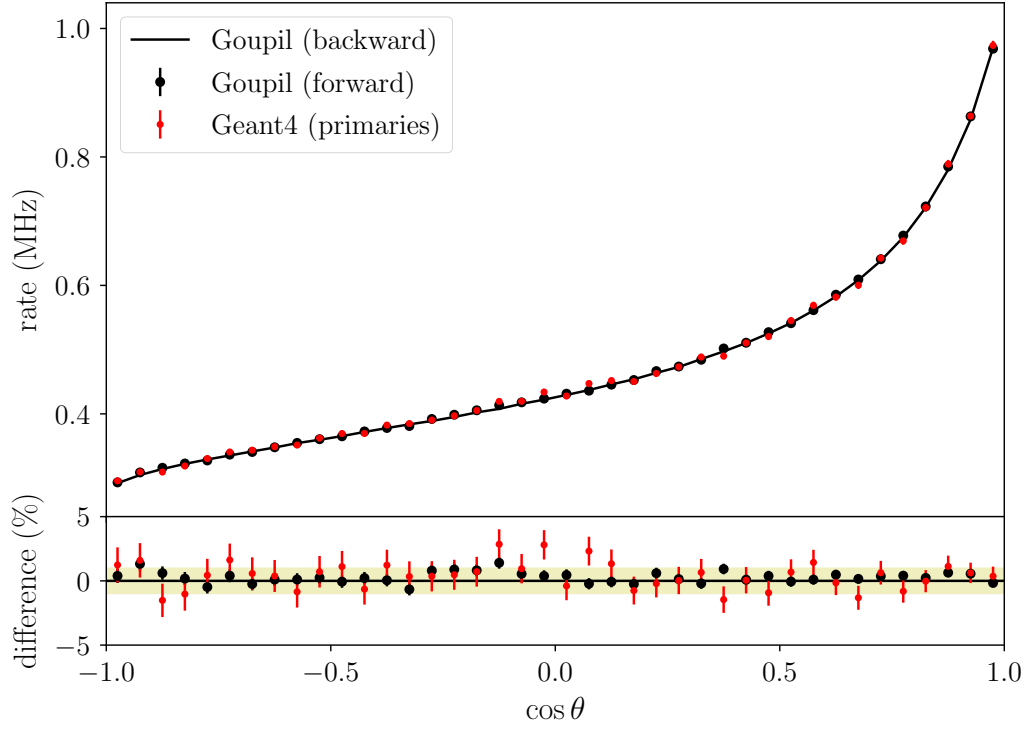


Figure 7: Deflection angle θ of background photons collected on the inner surface (\mathcal{C}) of the Test 1 geometry, relative to the direction of emission at the source. Monte Carlo uncertainties are indicated by error bars at 68% confidence. The lower inset shows the relative deviation w.r.t. the results obtained with GOUPIIL used in backward mode. The yellow band indicates a relative deviation of less than 1%.

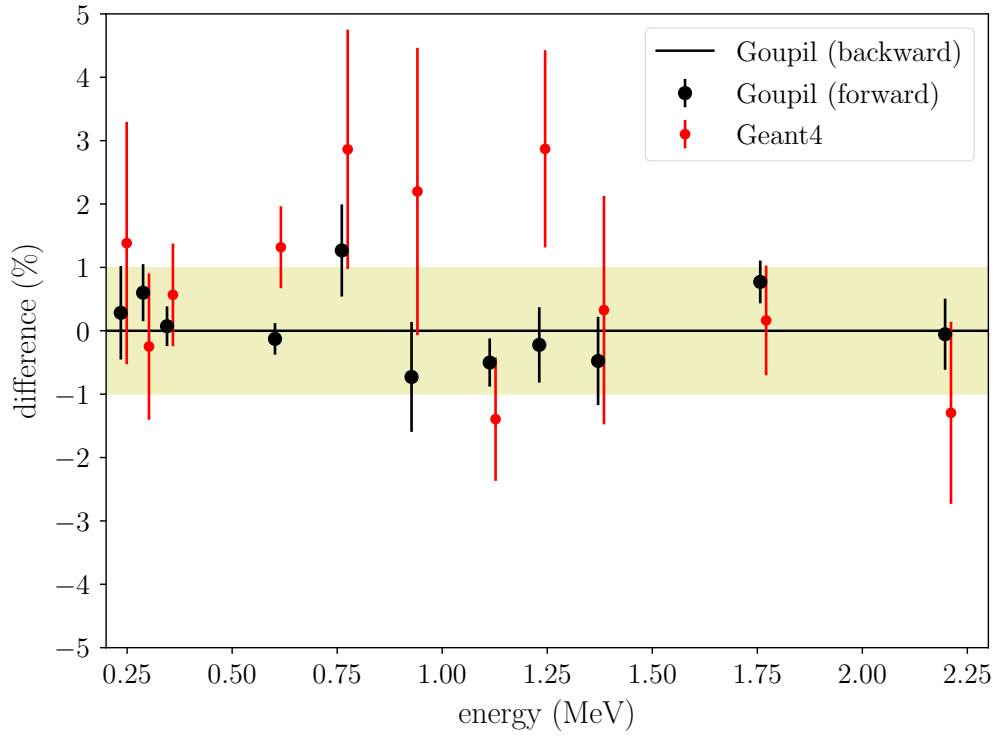


Figure 8: Relative differences (w.r.t. Goupil backward) in the intensities R_k of the photo-peaks observed on the collection surface \mathcal{C} of the Test 1 geometry. Error bars indicate Monte Carlo uncertainties (at 68% confidence). In the case of Goupil backward, these uncertainties are less than 0.5%. The yellow band indicates a relative deviation of less than 1%.

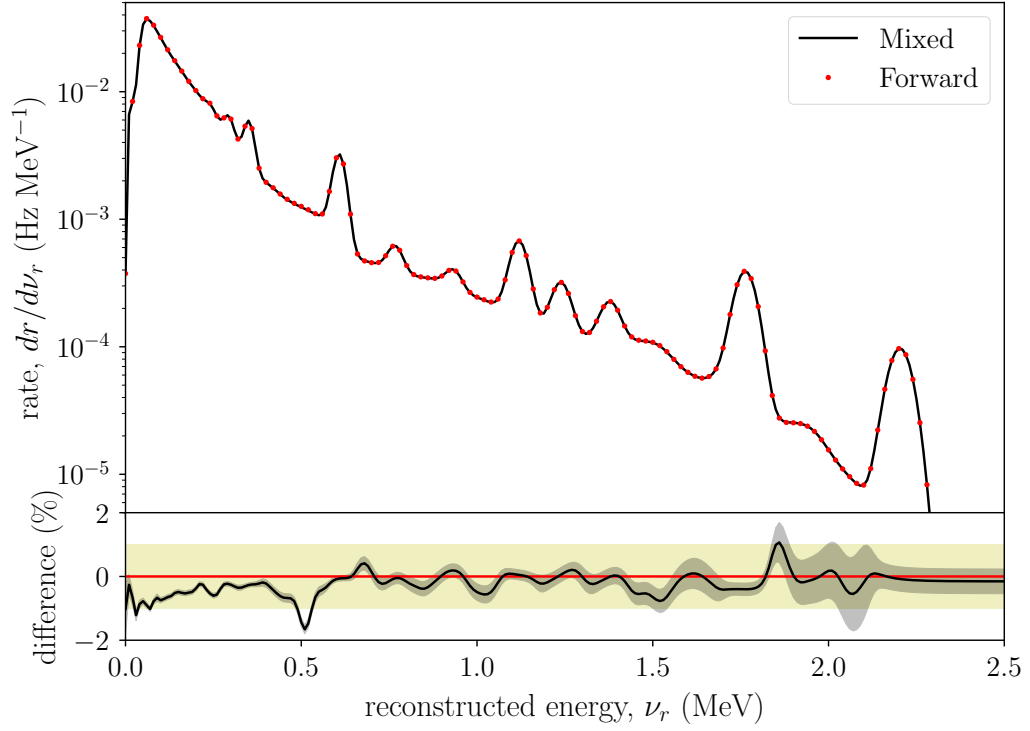


Figure 9: Differential counting rates ($dR/d\nu_r$) obtained with the Test 2 geometry. The bottom inset displays the relative deviation of the mixed procedure w.r.t. the end-to-end forward GEANT4 simulation. The yellow band indicates a relative deviation of less than 1%. The black shaded area represents the Monte Carlo uncertainties at 68% confidence (which are correlated due to the convolution with the detector response).

Algorithm 4 Constrained Backward Collision using a Russian Roulette method.

Require: $\nu_I > \nu_i > 0$, $q \in [0, 1]$, \mathcal{R} (a random stream).

```

1:  $\zeta \leftarrow \text{OPEN01}(\mathcal{R})$ 
2: if  $\zeta \leq q$  then
3:    $p_c \leftarrow \text{PDFFORWARD}(\nu_i, \nu_I)$ 
4:    $\omega_c \leftarrow \frac{p_c}{q}$ 
5:   return  $(\nu_I, \omega_c)$ 
6: else
7:   loop
8:      $(\nu_{i-1}, \omega_c) = \text{RANDOMISEBACKWARD}(\nu_i, \mathcal{R})$ 
9:     if  $\nu_{i-1} < \nu_I$  then
10:       $P_c^* \leftarrow \text{CDFBACKWARD}(\nu_I, \nu_i)$ 
11:       $\omega_c \leftarrow \frac{\omega_c P_c^*}{(1-q)}$ 
12:      return  $(\nu_{i-1}, \omega_c)$ 
13:     end if
14:   end loop
15: end if

```

Algorithm 5 Sampling of $\cos \theta$ in a Rayleigh collision.

Require: $q_0^2 > 0$, $\nu > 0$, \mathcal{R} (a random stream).

```

1:  $x_{\max} \leftarrow \frac{4\nu^2}{q_0^2}$ 
2: loop
3:    $\zeta \leftarrow \text{OPEN01}(\mathcal{R})$ 
4:    $x \leftarrow \frac{\zeta x_{\max}}{1+(1-\zeta)x_{\max}}$ 
5:    $q \leftarrow \sqrt{x q_0^2}$ 
6:    $f = \text{FORMFACTOR}(q, Z)$ 
7:    $g = \frac{1}{1+x}$ 
8:    $\cos \theta = 1 - 2 \frac{x}{x_{\max}^2}$ 
9:    $r = \frac{1+\cos^2 \theta}{2} \left[ \frac{f}{g} \right]^2$ 
10:   $\xi \leftarrow \text{OPEN01}(\mathcal{R})$ 
11:  if  $\xi \leq r$  then
12:    return  $\cos \theta$ 
13:  end if
14: end loop

```
